

ELECTRONIC AND CRYSTALLINE CHARACTERISTICS OF MIXED METAL
HALIDE PEROVSKITE SEMICONDUCTOR FILMS

A Thesis submitted in partial fulfillment of the
requirements for the degree of
Master of Science in Materials Science and Engineering

By

PATRICK JOSEPH CLEAVER

B.S. MSE, University of Minnesota, 2008

2018

Wright State University

WRIGHT STATE UNIVERSITY
GRADUATE SCHOOL

December 12, 2018

I HEREBY RECOMMEND THAT THE THESIS PREPARED UNDER MY SUPERVISION BY Patrick Joseph Cleaver ENTITLED Electronic and Crystalline Characteristics of Mixed Metal Halide Perovskite Semiconductor Films BE ACCEPTED IN PARTIAL FULFILLMENT OF THE REQUIREMENTS FOR THE DEGREE OF Master of Science in Materials Science and Engineering.

Hong Huang, Ph.D.
Thesis Director

Joseph C. Slater, Ph.D., P.E.
Chair, Department of
Mechanical and Materials
Engineering

Committee on Final Examination:

Hong Huang, Ph.D.

Maher S. Amer, Ph.D.

Suzanne K. Lunsford, Ph.D.

Barry Milligan, Ph.D.
Interim Dean of the Graduate School

ABSTRACT

Cleaver, Patrick Joseph. M.S.M.S.E., Department of Mechanical and Materials Engineering, Wright State University, 2018. Electronic and Crystalline Characteristics of Mixed Metal Halide Perovskite Semiconductor Films

Solar technology has a long history of incremental improvements in cost, reliability and efficiency. However, solar cells based on lead halide perovskite films have made more rapid leaps forward in the past 10 years, making it the fastest growing solar technology in terms of efficiency. Leaders in academia and industry continue to find success in overcoming manufacturability and stability issues, but have not yet discovered a high-efficiency perovskite film without the use of toxic lead.

Probing less toxic analogs to the highly efficient lead halide, a series of thin films with perovskite structures, i.e. $A_2BB'X_6$ where $A = \text{Cs}$ or FA , $B/B' = \text{Sn, Bi, Sb, Ag, and/or In}$ and $X = \text{I}$, are fabricated using a mixed metal approach. XRD patterns reveal the low dimensional $\text{A}_3\text{Bi}_2\text{I}_9$ crystal. UV/Vis spectra results show that the bandgap of bismuth-based perovskites is finely tuned, which has potential applications in future solar cells.

TABLE OF CONTENTS

1. Photovoltaics.....	1
1.1 Historical Background.....	3
1.2 Solar Cell Working Principle	6
1.2.1 Basics of Semiconductors.....	6
1.2.2 Photovoltaic Effect in Semiconductors	10
1.3 Classes of Solar Cells.....	13
1.3.1 Crystalline Silicon Solar Cells.....	13
1.3.2 III-V Semiconductor Solar Cells	14
1.3.3 Thin Film Solar Cells	16
1.3.3.1 a-Si:H	16
1.3.3.2 CdTe.....	17
1.3.3.3 CIGS	17
1.3.3.4 Organic Solar Cells.....	18
1.3.3.5 Dye-Sensitized Solar Cells	19
1.3.3.6 Perovskite Solar Cells.....	19
1.4 Objective of This Research and Overview of This Thesis.....	21
2. Metal Halide Perovskite Semiconductors.....	22
2.1 Materials and Structure	22

2.2 Synthesis of Hybrid Perovskites	26
2.2.1 Solution-based Synthesis	26
2.2.2 Vapor Deposition.....	32
2.2.3 Single Crystal Growth	32
2.2.4 Inverse Solubility Crystal Growth.....	32
2.2.5 Mechano-synthesis.....	33
2.3 Perovskite Film Characterization	33
2.4 J-V Performance of the PSC Device	35
2.5 Stability	37
3. Fabrication and Characterization of Pb-free Halide Perovskites	39
3.1 Background	39
3.2 Low-Toxicity Perovskite Film Fabrication	43
3.2.1 Organic FAI Synthesis.....	43
3.2.2 FAPbI ₃ Precursor	44
3.2.3 FASnI ₃ Precursor	44
3.2.4 Lead-free Precursors.....	44
3.2.4.1 CsI.....	45
3.2.4.2 BiI ₃	45
3.2.4.3 SbI ₃	45
3.2.4.4 AgI	45

3.2.4.5 InI.....	46
3.3 Perovskite Film Characterization.....	46
3.3.1 UV/Vis Spectroscopy.....	46
3.3.2 X-Ray Diffraction.....	47
3.4 Results and Discussion.....	48
3.4.1 Lead-Tin Mixed Films.....	48
3.4.1.1 FAPbI ₃	48
3.4.1.2 FASnI ₃	48
3.4.1.3 FA ₂ PbSnI ₆	49
3.4.2 Mixed Metal (In, Sb and Bi) films.....	50
3.4.3 Tin-alloyed FA Bismuth-Indium film.....	52
3.4.4 Cesium Bismuth-Indium Perovskite.....	54
3.4.5 Low-Dimensional Bismuth Perovskite.....	55
3.4.5.1 Cs ₃ Bi ₂ I ₉	55
3.4.5.2 FA ₃ Bi ₂ I ₉	55
3.4.6 Antimony alloying of Low-Dimensional Bismuth Perovskite.....	58
3.4.6.1 Cs ₃ Bi _{2-x} Sb _x I ₉	58
3.4.6.2 FA ₃ Bi _{2-x} Sb _x I ₉	58
3.4.7 Low-Dimensional Antimony Perovskite.....	65
3.4.7.1 FA ₃ Sb ₂ I ₉	65

3.4.7.2 Cs ₃ Sb ₂ I ₉	65
4. Conclusion	68
5. References.....	71
6. Appendix.....	78

LIST OF FIGURES

Figure 1. 1: Annual global photovoltaic new build capacity, 2006-2016 with 2016 Tier-1 capacity and forecast to 2019. ²	2
Figure 2. 1: Crystal Structure and common elements and molecular ions used in high performance metal halide perovskite solar cells ²⁹	23
Figure 2. 2: Schematic of nano-structured heterojunction device architecture (left), planar heterojunction device architecture (middle) and inverted heterojunction device architecture (right). ³⁶	24
Figure 2. 3: LaMer curve (a) where C_c is critical nucleation concentration, C_s is saturation concentration (b) slow evaporation (c) fast evaporation. ⁴⁴	28
Figure 2. 4: SEM images of MAPbI ₃ perovskite thin films, showing both solution based growth and colloidal based growth with orientated attachment. ⁴⁵	29
Figure 3. 1: UV-Vis Spectrum of combination of FAI, SnI ₂ and PbI ₂ in a 3:1:1 stoichiometric ratio. Vertical lines indicate an observed increase in absorption, indicating an electronic bandgap.	49
Figure 3. 2: UV-Vis Absorption and Tauc Plot for combination of FAI, BiI ₃ and InI precursors. Bandgap estimation is intercept of fit line (red) in inset Tauc Plot.	51
Figure 3. 3: XRD pattern of combination of FAI, BiI ₃ and InI with reference peaks labeled by black vertical lines. Peaks labeled with an asterisks (*) are attributed to BiI ₃ based on reference peaks in Appendix. The peak labeled (***) is unidentified.	52
Figure 3. 4: Plot of Estimated Bandgap vs. mol % of Tin precursor in films synthesized by combination of FAI, BiI ₃ and InI.	53
Figure 3. 5: UV-Vis spectrum for combination of CsI, BiI ₃ and InI with estimated bandgap at 2.25 eV.	54
Figure 3. 6: XRD pattern for combination of CsI, BiI ₃ and InI with reference peaks of Cs ₃ Bi ₂ I ₉ as black vertical lines. Peaks labeled with an asterisks (*) are attributed to CsI based on reference peaks in Appendix.	55
Figure 3. 7: UV-Vis spectrum for combination of CsI and BiI ₃ in a 3:2 stoichiometric ratio with an estimated bandgap at 2.3 eV.	56
Figure 3. 8: XRD pattern of 3:2 ratio of CsI and BiI ₃ . Reference peaks of Cs ₃ Bi ₂ I ₉ are tall vertical black lines. (*) indicates a BiI ₃ reference peak. Peaks labeled with an asterisks (*) are attributed to CsI based on reference peaks in Appendix.	57

Figure 3. 9: UV-Vis spectrum and inset Tauc Plot for 3:2 ratio of FAI and BiI ₃ with estimated bandgap at 2.31 eV.	57
Figure 3. 10: XRD pattern of 3:2 ratio of FAI and BiI ₃ . Reference peaks of FA ₃ Bi ₂ I ₉ are tall vertical black lines.	58
Figure 3. 11: UV-Vis spectrum for CsI, BiI ₃ , SbI ₃ where x = 0.3.	59
Figure 3. 12: XRD pattern for CsI, BiI ₃ , SbI ₃ in a 3:1-x:x stoichiometric ratio where x = 0.3. Peaks labeled with an asterisks (*) are attributed to CsI based on reference peaks in Appendix. Vertical lines are reference peaks for Cs ₃ Bi ₂ I ₉	60
Figure 3. 13: UV-Vis spectrum for CsI, BiI ₃ , SbI ₃ in a 3:1-x:x stoichiometric ratio where x = 0.6.	61
Figure 3. 14: XRD pattern for CsI, BiI ₃ , SbI ₃ in a 3:1-x:x stoichiometric ratio where x = 0.6. Peaks labeled with an asterisks (*) are attributed to CsI based on reference peaks in Appendix. Vertical lines are reference peaks for Cs ₃ Bi ₂ I ₉	62
Figure 3. 15: UV-Vis spectrum for FAI, BiI ₃ , SbI ₃ in a 3:1-x:x stoichiometric ratio where x = 0.3. Peaks labeled with an asterisks (*) are attributed to SbI ₃ and (***) are attributed to FAI based on reference peaks in Appendix. Vertical lines are reference peaks for FA ₃ Bi ₂ I ₉	62
Figure 3. 16: XRD pattern for FAI, BiI ₃ , SbI ₃ in a 3:1-x:x stoichiometric ratio where x = 0.3.	63
Figure 3. 17: UV-Vis spectrum for FAI, BiI ₃ , SbI ₃ in a 3:1-x:x stoichiometric ratio where x = 0.6.	64
Figure 3. 18: XRD pattern for FAI, BiI ₃ , SbI ₃ in a 3:1-x:x stoichiometric ratio where x = 0.6. Peaks labeled with an asterisks (*) are attributed to SbI ₃ and (***) are attributed to FAI based on reference peaks in Appendix. Vertical lines are reference peaks for FA ₃ Bi ₂ I ₉	64
Figure 3. 19: UV-Vis spectrum of FAI and SbI ₃ combined at a 3:2 ratio. Estimated bandgap is 2.3 eV.	66
Figure 3. 20: XRD pattern from combination of FAI and SbI ₃ in a 3:2 ratio. (*) indicates SbI ₃ peaks.	66
Figure 3. 21: UV-Vis spectrum of CsI and SbI ₃ with no bandgap determination.	67
Figure 3. 22: XRD pattern of CsI and SbI ₃ combined in a 3:2 ratio. (*) indicates SbI ₃ peaks and (***) indicates CsI peaks.	67
Figure 6. 1: UV-Vis spectrum of combination of FAI, SbI ₃ and InI.	78
Figure 6. 2: UV Vis spectrum of FAI, SbI ₃ and InI combined in a 3:1:1 stoichiometric ratio.	79

Figure 6. 3: UV-Vis spectra resulting from combination of FAI, BiI₃, InI and doping of x mol % SnI₂/0.2SnF₂ where x is a) 0, b) 0.08, c) 0.17, d) 0.25, e) 0.33, f) 0.42, g) 0.50, h) 0.58, i) 0.66, j) 0.75 and k) 0.83.80

LIST OF TABLES

Table 3. 1: Reference computed theoretical electronic band structure for possible double perovskites of the $A_2BB'I_6$ formula where A = FA, MA, Cs and B/B' = Bi, Sb, In, and Ag. Computation is based on spin-orbit hybrid HSE functional. ⁷¹	42
Table 3. 2: Annealing effects on estimated bandgap and detection of residual precursor phase.	51
Table 6. 1: Reference XRD peaks and corresponding crystal planes converted from Cr radiation source to Cu radiation source, used to compare experimental results to reference data. ⁷³	82
Table 6. 2: Reference XRD peaks for precursor materials, converted to Cr-source peaks for comparison to experimental data. ⁷³	82

ACKNOWLEDGEMENTS

I would like to thank my wife Norma for her support through this research project. I would like to thank Dr. Hong Huang for allowing me to work in her group and explore a new area of research. Thank you to my colleague, Ana Araujo of AK Steel for her assistance with X-Ray diffraction measurements. I appreciate very much the support of my committee members, Dr. Suzanne Lunsford and Dr. Maher Amer. They have provided thoughtful advice as I continued my education. I would also like thank Dr. Giles Eperon for his pioneering research and a detailed email correspondence which helped guide the setup of my research early on. Thank you to all researchers in this exciting field, I believe with continued innovation this technology can deliver more efficient and sustainable energy sources in our world.

1. Photovoltaics

Harvesting sufficient energy to power our ever-expanding and interconnected world is a challenge that will continue to grow into the future. At present, we are faced with supplying our energy needs using the commercial energy production technologies at hand. The desire to reduce the use of fossil fuels has contributed to an expansion of technologies that can be used to harvest, store and convert energy. Of these technologies, solar energy has received a large amount of attention due to its ability to collect free, natural sunlight that bombards the earth every day.

Currently, most commercial photovoltaic devices are made from high-purity silicon. Ingots are cast with ultra-low levels of impurities and subsequently sliced into wafers. These wafers are processed in clean facilities to reduce the risk of environmental contamination.¹ Many processes required the wafer to be placed in low-pressure chambers and complexity of manufacturing is high. While the cost of silicon solar cells continues to decline, there are still challenges in scaling global production to a significant level. Annual global solar capacity is approximately 100 gigawatts (GW) and forecasted to increase about 10% each year as seen in **Figure 1.1**.²

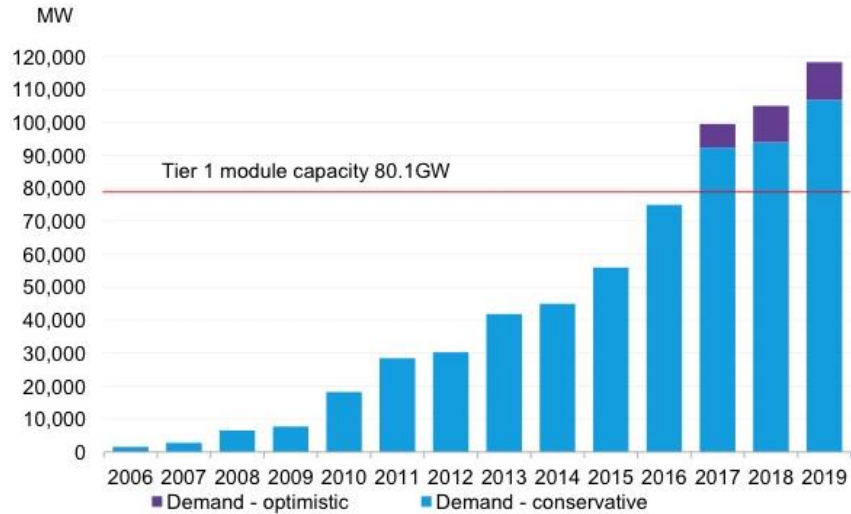


Figure 1. 2: Annual global photovoltaic new build capacity, 2006-2016 with 2016 Tier-1 capacity and forecast to 2019.²

Due to this relatively low amount of energy production capacity, solar energy continues to be a minor source of energy in our world. For solar energy to provide the world’s electricity needs, currently 20 terawatts (TW), it is estimated to take over one-hundred years to fabricate sufficient silicon-based solar cells.³

In recent years, there has been significant effort to create a solution-processable solar cell. One main advantage of this type of processing is the ability to fabricate solar cells quickly and cheaply by printing active materials in a roll-to-roll process. If we were able to match the current newspaper printing capabilities of the world with roll-to-roll solar cell production, the world’s energy need could be printed in a matter of years, not decades or centuries. This is the primary motivation of the current research into solution-processable photovoltaic systems.⁴

1.1 Historical Background

Edmond Becquerel, a 19-year old French scientist, created the first solar cell device while working in his father's laboratory in 1839. An acidic silver chloride solution was illuminated while platinum electrodes were submerged into the solution, generating a current.⁵ This phenomena was called the Becquerel effect, or more commonly known as the photovoltaic effect today.

In 1873, Willoughby Smith began working with Selenium while searching for a high-resistance material to be used in testing of underwater telegraph cables. In conducting his experiments, he seldom obtained the same results even under similar conditions. In further investigation of this discrepancy, it was found that the resistance of the material was affected by the intensity of incident light.⁶ This discovery would come to be known as the first display of Photoconductivity.

Charles Fritts, an American inventor, deposited a thin, transparent layer of gold onto selenium creating the world's first solid solar cell. He even installed a rooftop solar array in New York City in 1884.⁷ In spite of this development, little was well understood of a solar cell's working principles.

Around the same period, Philip Lenard, a German physicist was studying photoelectric effects of cathode ray tubes. He observed that the energy of the cathode ray increased proportional to the frequency of the light and was independent of the light intensity.⁵

This phenomenon would be further explained by Albert Einstein's *Annus Mirabilis* papers of 1905, offering a foundation of understanding by presenting the photoelectric effect. Einstein postulated that the energy of light is not continuously increasing but

rather consists of discrete energy quanta.⁸ The photovoltaic effect is built upon this understanding, where a sufficiently-high frequency of light must strike a photovoltaic material to allow for the excitation of an electron or charge carrier to a higher energy state.

Russel Ohl, an American engineer working for Bell Labs in Holmdel, NJ, had been revisiting the development of solid-state silicon crystal radio detectors for short wavelengths, needed for World War II era radar detection systems. It was common that these crystal detectors, made of commercial-grade silicon crystals, exhibited variable properties dependent on the precise location on the material and would result in directional rectification of radio signals. Ohl assumed the variability was due to the impurities in commercial-grade silicon crystal, often containing trace amounts of aluminum. Ohl began melting highly pure silicon powder under an inert Helium atmosphere in an effort to make highly pure silicon rods. In February 1940, testing was being performed on one of the many rods fabricated by Ohl's lab. This particular rod visibly showed a "change in crystal structure indicated by a crack".⁹ This rod also showed a more peculiar property, when exposed to light a current and relatively large voltage was generated. This unintentional crack marked a boundary between two regions of differing levels of silicon purities and would later be recognized as the first p-n junction. The 'p' region measured a positive voltage and the 'n' region measured a negative voltage. This discovery is not only the first silicon solar cell, but also laid the groundwork for the world-changing discovery of silicon transistors.

Development of the silicon solar cell rapidly accelerated at Bell Labs. Through experimentation with different dopants, Bell scientists arrived at a critical milestone in

1954, with a boron-doped silicon cell reaching a 6% efficiency of the solar spectrum.¹⁰ During this time, the limitations of the photovoltaic effect and its ability to harvest solar radiation spectrum was becoming better understood. The practice of referencing a percent efficiency began during this time. The efficiency was based on the terrestrial solar spectrum, the range of wavelengths generated by the sun that hits the earth.

Hoffman Electronics was given the technology developed by Bell Labs in order to advance the discovery and develop further applications. With the introduction of metal contact grids, Hoffman was able to achieve efficiencies of 14% in 1959.¹¹ In 1961, commercial solar cells with efficiencies as high as 15.2% found real-world applications in space satellites.¹¹ The rapid increase in efficiencies was highly motivated by the competitive space race between the US and the USSR.

The following decade would see a plateau in the development of silicon solar cells. Many scientists in the field pointed to the theoretical limit of efficiency as the reason for this stagnation. At this time the theoretical efficiency was estimated to be 22%. In 1973, this decade long dry spell was broken with fabrication of the “Violet Cell”, exhibiting an efficiency of 17.2%.¹² This achievement was made by creating a finer grid geometry and reducing the n-type layer thickness. The next year a “Black Cell” was made, which utilized a chemical etch to create a non-reflective surface by etching the {111} planes. In addition, these improvements were enhanced by alloying the rear layer with aluminum, creating a back surface field (BSF).¹¹ This aluminum back surface field (Al-BSF) architecture remains the most widely commercialized solar cell technology today.

Beginning in the 1980's and lasting until 2014, Martin Green's research group at the University of New South Wales has continued to push the solar efficiencies of single crystal silicon solar technology. Developments in this time period included development of the micro-grooved passivated emitter solar cell (PESC) in 1985. Key features of the PESC include an oxide layer on the top surface of the thin n-type layer of the cell combined with an intricate micro-grooved texture. The PESC cell demonstrated efficiencies above 20% with these improvements.¹³

Green would continue to push silicon solar technology toward more wide-spread commercialization through the fabrication of the passivated emitter and rear contact (PERC) cell. This cell was built off the PESC architecture and utilizes an oxide layer on the rear contact and employed an inverted pyramid texture. PERC technology has been projected to continually take market share away from Al-BSF technology and become the primary solar cell architecture in coming years.¹⁴

1.2 Solar Cell Working Principle

To understand the working principle of solar cells we need to understand what semiconductor materials are and why their properties are critical to the function of a working solar cell. The photovoltaic effect in semiconductors is at the core of the modern solar cell.

1.2.1 Basics of Semiconductors

The existence of a bandgap in non-metallic materials arises from the solution of the Schrödinger Equation for a given atom and is explained by molecular orbital theory. Semiconductors are defined by their electronic band structure, where there exists a

bandgap of less than 3 electron-volts (eV). The bandgap is defined as the difference between the highest occupied molecular orbital (HOMO) and the lowest unoccupied molecular orbital (LUMO). The HOMO and LUMO levels can also be referred to as the highest energy in the valence band and the lowest energy level of the conduction band, respectively.

The Pauli Exclusion Principle states that two electrons cannot occupy the same quantum energy state. This means that each energy level can be filled with a maximum of two electrons which have opposite quantum spin states. Using this principle, the electronic structure of the Si atom is shown to have 4 valence electrons. One electron resides in the 3s orbital and three electrons reside in the 3p_x, 3p_y and 3p_z orbitals.

In a Si crystal, each of the 4 valence electrons of an atom reside in a symmetric hybridized sp³ orbital, resulting in tetrahedral coordination in the structure. As the crystal structure forms, each sp³ molecular orbital approaches the molecular orbital of a neighboring Si atom. Each individual energy state of the sp³ molecular orbital is split in bonding, resulting in a bonding orbital of lower energy and an anti-bonding orbital of higher energy. Band energy splitting is an underlying principle which gives rise to the valence and conduction band. A pure Si crystal has a bandgap of 1.1 eV at 300 K.¹

The Fermi level, also referred to as the chemical potential of an electron, is defined as the energy level where an electron has a 50% probability of residing. For a pure, intrinsic, semiconductor, the Fermi level lies in the middle of the band gap. The probability of an electron occupying an energy state, ϵ , is given by the Fermi-Dirac equation (Equation 1),

$$f(\epsilon) = \frac{1}{e^{(\epsilon-\mu)/kT} + 1} \quad (1)$$

where μ is the Fermi level, k is Boltzmann's constant, and T is temperature (K).¹

At $T = 0$ K, the probability of an electron existing below the Fermi level is unity, meaning the valence band is entirely full of electrons and no electrons exist in the conduction band. By increasing T , above 0 K, negatively charged electrons begin to fill the conduction band and positively-charged holes are left behind in the valence band. In this way the number of mobile charge carriers, free electrons and free holes, are increased by increased temperature.

The Law of Mass Action states that, under thermal equilibrium, the concentration of holes, p , multiplied by the concentration of electrons, n , is equal to a constant squared.

$$np = n_i^2 \quad (2)$$

Equation 2 represents the charge carrier concentrations in intrinsic semiconductors.

The number of charge carriers can be manipulated by intentionally introducing impurities into material, called doping. When the vacancy of the dopant atom differs from the matrix atom, each dopant atom provides an additional charge carrier to the system, in the form of electrons or holes.

One common dopant in Si systems is phosphorus, P. Since P has five valence electrons, it will have one electron left over after bonding with four neighboring Si atoms. This dopant effectively adds electrons to the crystal and also adds allowable energy levels in the band structure, which lie inside the band gap. Since P is donating electrons, the

additional allowable energy band will be slightly below the conduction band. This crystal now has more electrons than holes, meaning electrons are the majority charge carrier, and this extrinsic (doped) semiconductor is called n-type.

Another dopant common to doped-Si is boron, B. Boron has 3 valence electrons and will fall short in contributing electrons to the Si crystal. Subsequently, a hole is created for each B atom introduced to the system. Doping of B adds an allowable energy level to the bandgap, which lies directly above the valence band. The number of holes in this p-type extrinsic semiconductor is much larger than the number of electrons, which are the minority charge carrier in this situation.

For extrinsic (doped) semiconductors, this equation can be related to the concentration of dopant. Equations 3-6 show this relationship for both n-type and p-type doping, assuming each atom of dopant donates or accepts one electron to or from the lattice.¹⁵

n-type doping:

$$N_D = n_0 \quad (3)$$

$$p_0 = \frac{(n_{intrinsic})^2}{n_0} \quad (4)$$

p-type doping:

$$N_A = p_0 \quad (5)$$

$$n_0 = \frac{(n_{intrinsic})^2}{p_0} \quad (6)$$

1.2.2 Photovoltaic Effect in Semiconductors

A solar cell depends on the movement of charge carriers. Considering a freely distributed electron gas, each electron has some kinetic energy with random vectors of motion. If all particles move randomly, there will be no net movement of electrons. In the presence of a density gradient, dn/dx , in the electron gas, the electron flux, J_e , can be described by Fick's Law of Diffusion, where q is the electron charge, D_e is the diffusion coefficient. Holes will also follow a similar principle with regards to diffusion, Equations 7-8.

$$J_e = qD_e \frac{dn}{dx} \quad (7)$$

$$J_h = qD_h \frac{dn}{dx} \quad (8)$$

Drift is another important transport phenomena that is relevant to the solar cell working principle. Drift can be described as the induced motion of charge carriers due to an applied electric field. The drift current density can be related to the applied electric field, E , by the Equations 9-10 for electrons and holes, respectively.

$$J_e = nq\mu_e E \quad (9)$$

$$J_h = pq\mu_h E \quad (10)$$

For electrons, q is the negative of the elementary charge. For holes, q is positive and equal to the absolute value of the elementary charge. This leads to the fact that drift for holes and electrons will have opposing vectors with respect to each other.

Most solar cells are based on p-n junctions. When an n-type material is placed next to a p-type material this creates such a junction. Consider this device free from light and in a thermal state of equilibrium. The n-type material will be negatively charged and the p-type material will be positively charged. This results in a local electric field, creating a depletion zone. This area has been depleted of any charge carriers and created the potential for drift of the region's minority charge carriers. The drift direction of a given charge carrier is opposite the diffusion direction. The diffusion is driven by the density of majority charge carriers and flows from the higher-density to lower-density side of the p-n junction.

If each side of the p-n junction is connected to create an electric circuit and is at thermal equilibrium, the depletion zone will stabilize and the Fermi levels will equalize. This results in a bending of the electronic band structure across the depletion zone. The difference in the Fermi levels of each region give rise to the built-in voltage, V_{bi} , of the p-n junction by Equation 13, where q is the charge of an electron.

$$E_{fn} - E_{fp} = qV_{bi} \quad (11)$$

We can manipulate the equilibrium that was previously assumed by applying a bias voltage across the junction or shining light on the junction. Forward bias applied across the junction effectively reduces the barrier to diffusion for charge carriers. The diffusion of charge carriers increases exponentially, while the depletion zone width and the built-in voltage decreases. Forward bias over the device generates a net current flow through the metal contacts. Reverse bias applied across the junction increases the size of the depletion zone and increases the barrier to diffusion, resulting in relatively low net

current. This device is considered a diode due to its rectifying current-voltage (JV) behavior. Equation 14 is the ideal diode equation which describes the current dependence on voltage of an ideal p-n junction diode in the dark.

$$J(V) = J_n + J_p = J_s \left(e^{\frac{qV}{kT}} - 1 \right) \quad (12)$$

Introducing thermal energy or shining light upon this diode will result in generation of charge carriers through thermal generation and photo-generation, respectively. We are most interested in photo-generation with respect to the application of solar power harvesting. Light is comprised of highly energetic, ultra-low mass particles called photons. When photons of sufficiently high energy collide with lattice bound electrons, they will be excited above the bandgap and generate a free electron and hole pair. This will increase the density of minority charge carriers in the n and p regions of the p-n junction. It can be predicted from Equation 14, that the charge carrier drift current density will be greatly increased under photon illumination. Many electrons will drift from the p-region to the n-region, while many holes will drift from the n-region to the p-region. This results in current generation across the device, which is the working principle of a solar cell.

After charge carriers are generated, it is possible that they do not add to power generation of a solar cell due to recombination. Charge carrier recombination can occur when an electron in the conduction band becomes close enough to a hole and the charge carriers combine and return to a bound state in the crystal lattice. The way in which the charge carriers recombine and transfer resultant energy define the type of recombination that occurs.

Radiative recombination occurs when an electron and hole recombine, as a result, a photon is ejected from the semiconductor. Auger recombination occurs when released energy is transferred to another electron and is subsequently excited to the conduction band. In Shockley-Read-Hall recombination, defect states can trap electrons for a longer period of time, causing them to recombine with a hole in the valence band. Diffusion length, L , is the average distance the charge carriers travel before recombination. It is related by Equations 11-12 to the charge carrier lifetime and a diffusion coefficient of the charge carrier through the lattice.

$$L_e = \sqrt{D_e \tau_e} \quad (13)$$

$$L_h = \sqrt{D_h \tau_h} \quad (14)$$

When the p-region is connected to the n-region, a voltage is built up as charge carriers accumulate on each side of the junction. This built up voltage is called the open circuit voltage. Under illumination a current can be measured, which is called the short circuit current. The short circuit current and the open circuit voltage are characteristic of a solar cells geometry, the light source used, quality of manufacture and the semiconductor material class.

1.3 Classes of Solar Cells

1.3.1 Crystalline Silicon Solar Cells

The crystalline silicon (c-Si) solar cell is the most mature solar technology. Crystalline solar technology is utilized for approximately 90% of global solar cell production. Cells made from crystalline, wafer-based silicon have a proven lifetime over 25 years with

little degradation under typical operational conditions. The bandgap of a c-Si cell is 1.12 eV, which is less than the ideal bandgap of 1.34 eV, determined by the solar spectrum. The bandgap of c-Si is indirect and charge carriers must be both energized and given some momentum to be excited to an unbound state. Even with the less than optimal bandgap characteristics, c-Si is still the most efficient, mass-produced solar technology available commercially.

Based on the source of silicon, c-Si technology can be considered single-crystal silicon (sc-Si) or multi-crystalline (mc-Si). All c-Si cells are made from wafers of silicon, which are cut from larger bulk Si materials. Boules, made most commonly by the Czochralski process, are perfect single crystals, meaning there are no grain boundaries throughout the entire bulk of material. The Si single crystals are carefully manufactured to have ultra-low levels of unintentional impurities. These single crystal wafers are typically doped to be n-type and made into sc-Si solar cells.

Alternatively, cast multi-crystalline ingots are made into large rectangular forms, from metallurgical grade silicon, typically by the Siemens process. Wafers made from multi-crystalline silicon ingots have lower manufacturing costs than single crystals and are most often made to be p-type. Random grains are formed in the process and grain boundaries exist in the bulk of the material, which leads to a higher rate of recombination and ultimately lower efficiency when compared to sc-Si cells.¹⁶

1.3.2 III-V Semiconductor Solar Cells

III-V semiconductor materials are combinations of group-III elements (ie. Al, Ga, In) and group-V elements (ie. N, P, As, Sb). GaAs is the most prevalent binary system in

photovoltaic applications. There are also many ternary and quaternary systems that include GaInAs, GaInP and AlGaInAs. III-V semiconductors often demonstrate the highest efficiencies in solar cells due to their direct band gaps, high absorption coefficients and low non-radiative recombination rates.

Multi-junction solar cell devices based on III-V semiconductor materials, achieve the highest efficiencies compared to other photovoltaic devices. The high efficiencies are achieved by stacking layers of varying bandgaps, allowing for more efficient light absorption in multiple wavelength ranges. III-V semiconductors are able to be formulated in a wide variety of combinations and stoichiometric ratios, making it possible to engineer specific band gaps in order to optimize performance of multi-junction solar cells.

A main drawback to this class of materials is the need for rare and toxic elements as well as expensive epitaxial deposition methods. These factors drive up the cost of manufacture significantly. Manufacturing costs of multi-junction solar cells adds to their high price and limits their practical use to outer space and high-concentration photovoltaic (HCPV) systems. In HCPV systems, mirrors and lenses concentrate sunlight onto relatively small and very high efficiency multi-junction solar cells. While cooling systems and sun-tracking systems are an added cost for HCPV operations, lower required area of the active photovoltaic cell can offset these costs. Development of concentration PV systems continues and may become competitive with conventional silicon based PV technology for utility scale power in coming years.¹⁷

1.3.3 Thin Film Solar Cells

In an effort to reduce the cost per Watt of solar cells and become competitive with crystalline Si, thin film technologies have been developed. Some key advantages of thin film solar cells include lower material costs and ability to deposit them onto transparent and/or flexible substrates. Thin film photovoltaic material systems have been shown to produce increasingly efficient solar cells.

1.3.3.1 a-Si:H

Hydrogenated amorphous silicon (a-Si:H) is used to produce thin film solar cells. Compared to crystalline Si cells, the a-Si:H cells show stronger absorption due the shift from an indirect band gap to a direct bandgap. The electronic bandgap of a-Si:H ranges from 1.6 eV to 1.9 eV, depending on the hydrogen-doping level. This is higher than the optimal bandgap based on the solar spectrum which reduced its competitiveness with lower band gap materials. Another drawback is caused by its amorphous structure, due to the presence of dangling bonds which act as recombination-causing defects in the material.

Thin film a-Si:H cells can be combined with lower bandgap hydrogenated nano-crystalline silicon nc-Si:H to increase the efficiency of multi-junction cells, from low-cost and non-toxic materials. These cells are termed micro-morph double junction cells.

Success of these cells are limited by their relatively low efficiencies compared to other thin film materials as well as their poor stability due to light induced degradation by the Staebler-Wronski effect.¹⁸

1.3.3.2 CdTe

The leading commercial thin film technology is made from the cadmium-telluride semiconductor. CdTe is well suited for absorption of sunlight due to its direct bandgap of 1.45 eV. Due to the strong absorption coefficient of CdTe, only a few microns of material is needed to absorb over 90% of incident photons. The n-type region is made up of a CdS layer and the p-type CdTe layer is deposited on top, creating the active junction. The high level of stability in CdS/CdTe cells has been proven, due to the passivated and high-bonding strength of the CdTe crystal.

CdTe can be processed by a variety of techniques including close-spaced sublimation (CSS), screen printing and electrodeposition. This is a key factor in reducing the cost per Watt of CdTe solar cells. It is currently the least expensive photovoltaic material per Watt. Key drawbacks include the need for highly-toxic elemental cadmium as well as scarcity of tellurium, which could limit its ability to move to mass production.¹⁸

1.3.3.3 CIGS

Copper indium gallium diselenide (CIGS) alloys have a direct band gap with a large absorption coefficient, which allows for thin layers of 1-2 microns to absorb a large portion on incoming light. The crystal formula is $\text{CuIn}_x\text{Ga}_{1-x}\text{Se}_2$, where the bandgap is 1.0 eV when $x = 1$ and 1.7 eV when $x = 0$. Depending on the stoichiometric ratio of In and Ga, the bandgap can be tuned between these values. CIGS solar cells have the highest reported lab efficiencies of the previously discussed thin film technologies. CIGS films, like CdTe, can be deposited in a wide variety of processing technique, like co-evaporation and sputtering.

Consistent processing methods are difficult to prove out industrially due to the sensitivity of CIGS active layers to stoichiometric tolerances. Like CdTe, toxicity of cadmium is a concern and scarcity of indium may also be a limiting factor in future deployment. Commercialization has stagnated for CIGS technology in recent years due to cost advantages of CdTe, which is also a more mature technology industrially.¹⁸

1.3.3.4 Organic Solar Cells

The organic bulk heterojunction (BHJ) photovoltaic system has proven to be a promising candidate for solution-processable photovoltaics. In organic solar cells, conjugated polymers are designed to act like doped semiconductor materials. Instead of truly free electrons and free hole pairs acting as the charge carriers, excitons are the product of light absorption. An exciton is a quasiparticle consisting of a hole and electron bound by a relatively weak Coulombic force. The exciton lifetimes are relatively short compared to unbound electrons and hole pairs, leading to shorter diffusion lengths. The excitons diffuse through the active layer to the interface between the n-type donor layer and the p-type acceptor layer. The exciton is separated at the layer interface, into free electrons and free holes, which travel out of the device through the electrodes for charge extraction and current generation.

Organic photovoltaics (OPV) are optimized by increasing interfacial area between the donor and acceptor materials. Since the diffusion lengths are very short, smaller distances between any given point in the active layer and an interface results in improved cell performance. While there are a wide variety of polymer materials used in OPVs, one heavily studied OPV system is that of poly (3-hexylthiophene-2,5-diyl (P3HT) and phenyl-C61-butyric acid methyl ester (PCBM). One of the largest hurdles for BHJ's is

the recombination of excitons before they are able to reach the extraction layers. The exact mechanisms of charge transport in these very complex material systems continue to be investigated in hopes to increase the efficiency and commercial viability of OPVs.¹⁹

1.3.3.5 Dye-Sensitized Solar Cells

Dye-sensitized solar cells (DSSCs) were first introduced as a low-cost, high-efficiency solar cell by Michael Grätzel in 1991. The DSSC is a photoelectrochemical device which uses a sensitizer as absorber and electron donor. It is made with a wide bandgap semiconductor, typically of TiO₂ nanoparticles, which acts as the electron acceptor. Electrons travel through the circuit and arrive at the catalyzed counter electrode, often made with platinum and a conductive oxide. A redox electrolyte is employed to facilitate current generation across the device, by reacting with the electrons at the counter electrode and replenishing electrons to the dye-sensitizer molecules. A typical redox electrolyte is a liquid I⁻/I₃⁻ solution made of iodine, an iodide salt and carried in a glycol. Challenges of DSSC's include cost of the Pt electrode, stability of electrolytes and the spectral optimization of the dye-sensitizer materials.²⁰

1.3.3.6 Perovskite Solar Cells

In 2009, Miyosaka demonstrated a dye-sensitized solar cell (DSSC) using the hybrid (organic-inorganic) perovskite CH₃NH₃PbI₃ as the sensitizer on a TiO₂ mesoporous structure. While the power conversion efficiency (PCE) of 3.8% was admirable for a preliminary DSSC using a new sensitizer, the device lifetime was very short due to the rapid degradation of the perovskite crystal in contact with the liquid iodide/triiodide redox electrolyte.²¹ For this reason, this discovery did not receive much attention. In 2012, Park fabricated a device that utilized a solid-state spiro-MeOTAD hole conducting

layer, which proved to be stable and displayed a PCE exceeding 9%.²² The solid-state devices showed relatively fast charge transport in comparison with other dye-sensitized cells. Concurrently, Snaith changed the n-type conductive TiO₂ mesoporous structure with an insulating Al₂O₃ mesoporous structure, in an effort probe for charge transport in the perovskite layer.²³ Surprisingly, the cells incorporating an electrically insulating Al₂O₃ mesoporous scaffold showed an improved PCE of 10.9%, due the forced transport of electrons through the perovskite material itself.

This demonstrated that the hybrid perovskite not only functioned as a light absorber but also as an electron transport material, enabling hybrid perovskite cells to be conceived as a stand-alone class of photovoltaic devices, outside the DSSC classification. In 2013, Snaith demonstrated efficiencies as high as 15.4% using a planar heterojunction architecture, officially making perovskite solar cells (PSC) a solar material class of its own.²⁴ This sparked interest within solar research groups and rigorous research began, investigating the fundamental mechanisms of perovskite materials as light absorbers.

The development of planar heterojunction architectures followed, the high efficiencies reported were explained by several studies showing relatively high electron-hole diffusion lengths. This fact was combined with relatively high absorption coefficients, allowing for thinner films to be sufficient for absorption of a wide range of wavelengths. High electron-hole diffusion lengths enable higher efficiencies since the holes and electrons are more likely to be collected by their relative transport layers rather than recombining in the device.²⁵

1.4 Objective of This Research and Overview of This Thesis

The combination of low cost materials, inexpensive processing methods and high performance makes the hybrid PSC highly competitive to silicon and other thin film technologies. Its primary challenges are device stability and toxicity of precursor materials. There have been significant improvements in stability, by both improved material selection and film deposition methods. The toxicity issue is addressed by encapsulation, but without completely removing toxic Pb from perovskites, the hazard to human health remains a barrier to widespread commercialization.

The objective of the current research was to learn about processing lead halide perovskite films and apply that knowledge to the fabrication of lead-free, low-toxicity alternatives. Better understanding of the widely studied lead halide perovskite material helped to guide this lead-free research by attempting to match the properties observed without using lead. Referencing several computational studies, performed by other groups, elements were chosen to be used in the exploration of new combinations of metal halide perovskites. Characterization methods were employed to help predict how well these materials will perform in a photoelectrical application, focusing on the photovoltaic application. This thesis explores the highly efficiency lead-based halide perovskite material and the current understanding its high performance as a light-harvesting thin film. Approaches to discover a lead-free alternative are explained. A series of material combinations are explored experimentally, the results are reported and compared to reference results. The current thesis shows a pathway forward to explore a particular series of materials that may result in improved photovoltaic performance compared to current lead-free perovskite materials.

2. Metal Halide Perovskite Semiconductors

2.1 Materials and Structure

The perovskite term was first used to describe the structure of CaTiO_3 which was discovered by Gustav Rose in 1839 and named after Russian scientist Count Lev Alekseevich Perovski.²⁶ Organic-inorganic halides were first crystalized and characterized in 1978 by Dieter Weber.²⁷ The hybrid perovskite's electronic properties were studied by Mitzi in the 1990's at IBM Research, showing semiconducting behavior of low-dimensional orientated sheets of the material.²⁸ At present, organo-lead halides are the most widely studied material system for hybrid perovskites used in photovoltaic applications. These materials are a combination of organic ions surrounded by an inorganic metal-halide framework, forming the perovskite crystal structure.

The hybrid perovskite used in solar cells follow the formula of ABX_3 , where X is a halogen (Cl, I, Br or a combination). Organic, methyl ammonium ions (CH_3NH_3^+ / MA^+), formamidinium ions ($\text{HC}(\text{NH}_2)_2^+$ / FA^+) or the inorganic cesium Cs^+ atom resides in the A location. On the B site Pb is typically used. It has been shown that Sn^{2+} or combinations of charge balanced metals can be used as a substitute and produce working PSCs. The structure is illustrated in **Figure 2.1**.²⁹

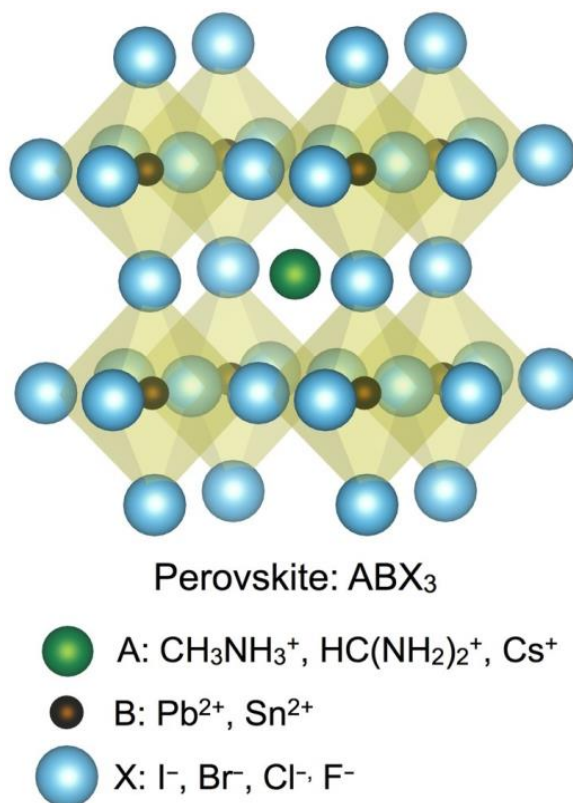


Figure 2. 1: Crystal structure and common elements and molecular ions used in high performance metal halide perovskite solar cells.²⁹

Metal halide perovskites use elements from the periodic table following the general formula I-II-VII₃. While the material system that is the focus of this thesis is lead-free, for the purposes of this chapter, the highly efficient and most widely studied lead based system will be considered. The monovalent cation used in most research is MA⁺, FA⁺ or Cs⁺. The effective radius of MA⁺ and FA⁺ are 2.17Å and 2.53Å, respectively.³⁰ The use of Cs⁺, an inorganic cation, with an ionic radius of 1.81Å, has been used as both a standalone cation and in mixed cationic configurations.³¹

The perovskite crystalline structure of MAPbI₃ exhibits three reversible phase transitions. The lowest temperature configuration is orthorhombic, assigned to the Pnma space group. The structure transforms to tetragonal, its room temperature configuration, above 161 K

and is of the $I4/mcm$ space group. As temperature increases to 327 K, the structure transforms continuously to a cubic structure of the $Pm\bar{3}m$ space group.³² The bandgaps of the $MAPbI_3$ crystal for its orthorhombic, tetrahedral and cubic phases are 1.61eV, 1.43eV and 1.30eV, respectively.^{33, 34, 35}

The organic cations in hybrid perovskites $MAPbI_3$ and $FAPbI_3$ have a dynamic crystal structure. The increase in degrees of freedom of the organic cation leads to the transitions mentioned above. The cation is able to increasingly rotate at higher temperatures, first in 2 dimensions and increasingly in 3 dimensions, leading to the high temperature cubic structure.³⁵

While the hybrid perovskite is an important material in emerging photovoltaic devices, there are a host of supporting materials used to produce working devices. Three main device architectures have been demonstrated, nano-structured heterojunction, planar heterojunction and inverted heterojunction, as seen in **Figure 2.2**.³⁶ All device architectures utilize a transparent substrate with a transparent conductive oxide (TCO) layer, like fluorine-doped tin oxide (FTO).

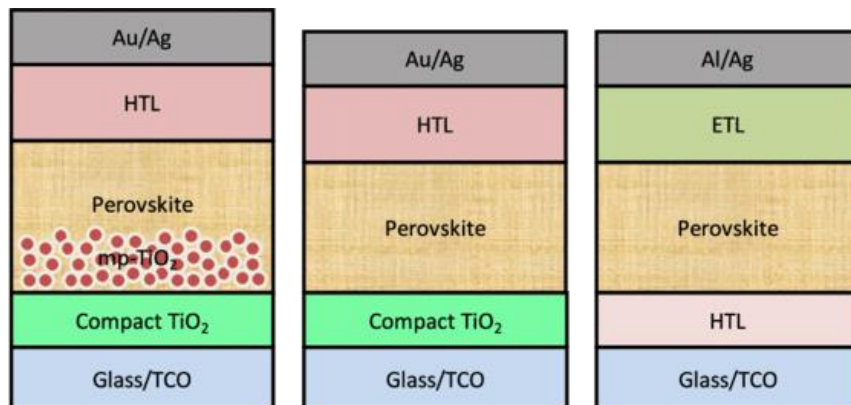


Figure 2. 2: Schematic of nano-structured heterojunction device architecture (left), planar heterojunction device architecture (middle) and inverted heterojunction device architecture (right).³⁶

The nano-structured heterojunction cell is commonly constructed off of a nano-structured mesoporous TiO₂ layer on top of a metal oxide compact electron transport layer. The mesoporous nanostructure allows for high surface area to extract electrons from the absorber layer. The absorber layer is a polycrystalline hybrid perovskite in its variety of formulations described in this review. Deposited on top of the perovskite layer is a hole conduction layer which is commonly made up of spiro-MeOTAD, (2,2',7,7'-tetrakis-(N,N-di-p-methoxyphenylamine)-9,9(spirobifluorene)). To complete the device a sputtered layer of Au or Ag is deposited.

In the planar thin film architecture, a compact layer of TiO₂ is put on top of a transparent conductive glass. The perovskite is deposited on top of this layer as a thin film. While hole transport layer of spiro-MeOTAD is typical, devices have also been constructed using polymer hole conductors like PEDOT:PSS poly (3,4-ethylenedioxythiophene) poly (styrenesulphonate). Utilizing electronic polymers allows for the possibility to construct flexible devices which are advantageous for certain applications.³⁷

Inverted devices are constructed with a hole transport layer (HTL) between the transparent conductive oxide (TCO) and the perovskite layer. The electron transport layer (ETL) is then deposited on top of the perovskite and metal contacts are deposited on top of the ETL. The inverted p-i-n configuration has been found to enhance hole extraction and reduce the hysteresis effect that is common in perovskite solar cells (PSCs). The alternative inverted architecture also provides flexibility in design of tandem cells, i.e. CIGS/PSC or c-Si/PSC tandem solar cells.³⁸

2.2 Synthesis of Hybrid Perovskites

The perovskite's ability to absorb and extract charge to the device electrodes is highly influenced by the crystal formed and the resultant film morphology.³⁹⁻⁴² Various methods have been employed and studied extensively in the last few years as interest in the field accelerates. Methods of hybrid perovskite fabrication include one-step and two-step deposition methods based on solution processing, vacuum deposition methods, or a combination of vapor deposition and solution processing.²⁵

2.2.1 Solution-based Synthesis

A major competitive advantage for perovskite solar cells is the ability to be processed from solution in more cost effective ways. The most common synthesis route has been the one-step or two-step solution deposition by spin coating and subsequent annealing/evaporation at temperatures ranging from 25 - 200°C. Most research is currently done inside a glove box under an inert atmosphere, while some studies have shown low, controlled humidity to be beneficial in film formation.⁴³

All PSC device architectures discussed previously can incorporate solution-based processing methods in their fabrication. For instance, hole and electron transport layers of various materials can utilize simple solution-based processing methods. The electron transport layer of compact TiO₂ can be fabricated by spray pyrolysis or spin coating onto the conductive glass substrate. Typically the coating process is followed by a high temperature sintering step around 500°C. Hole transport layers of spiro-MeOTAD or PEDOT:PSS can be solution processed at room temperature by spin coating. Metal contact layers are typically deposited using thermal evaporation methods.

Researchers have found rapid improvement in device performance by tuning the temperatures, times and annealing atmospheres. Adding various solvents or additives to precursor solutions have been investigated in efforts to improve the final film morphology. The ability to use a variety of formation techniques is assisted by the relatively fast reaction rates between the organic (methyl ammonium halide) and inorganic (lead halide) species. On the other hand, the dissimilar properties of the organic and inorganic species pose a difficult task of finding appropriate solvents and processing conditions that do not sacrifice the integrity of the final perovskite layer.

One-step vapor deposition involves a dual source of the organic precursor (i.e. MAI) and the inorganic metal halide (i.e. PbI_2). This process can be challenging since each source must be held at different temperatures during the formation process.

One-step solution processing is carried out by dissolving the organic and inorganic species into an organic solvent and depositing onto the substrate, thermal annealing follows to complete the crystal formation. A challenge of this method is film shrinkage as solvents are evaporated away.

Two-step processing can also be used to form the perovskite by first depositing the metal halide salt, i.e. PbI_2 , followed by a sequential deposition of the organic species, i.e. MAI. This method includes a subsequent annealing step where the perovskite crystal is formed. A combined solution/vapor deposition method can also be employed where the metal halide is solution deposited, followed by vapor deposition of the organic species. The two-step method can also involve a metal halide film cast first and the organic halide

subsequently added. This process physically expands the volume of the original film, typically resulting in a rougher surface structure.²⁵

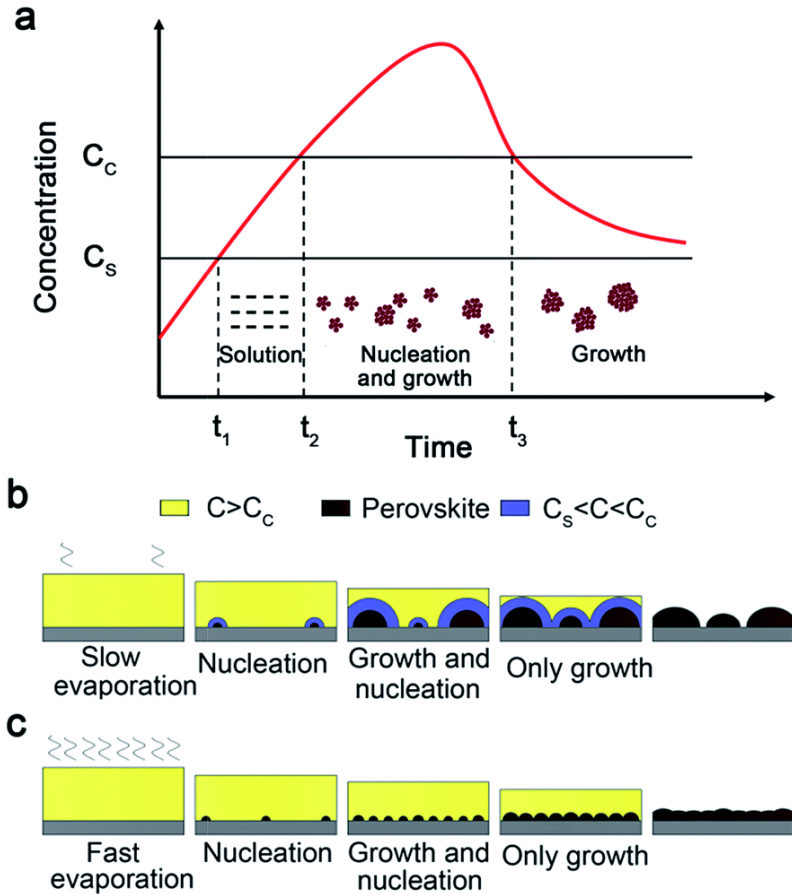


Figure 2. 3: LaMer curve (a) where C_c is critical nucleation concentration, C_s is saturation concentration (b) slow evaporation (c) fast evaporation.⁴⁴

Basic understanding of the formation of perovskite thin films can be described as a supersaturated solution that initiates heterogeneous nucleation and subsequent crystal growth. This has been described through the LaMer curve as seen in **Figure 2.3**.⁴⁴

Following the red curve, the increase in concentration to a point above the C_c , critical concentration initiates the formation of crystal nuclei. Consumption of the crystallizing

species increases as more nucleation and crystal growth occurs, resulting in a decrease in concentration. The crystal growth of existing nuclei continue until all the solute is consumed. Below the curve in **Figure 2.3**, the evaporation rate influence on film morphology is depicted.

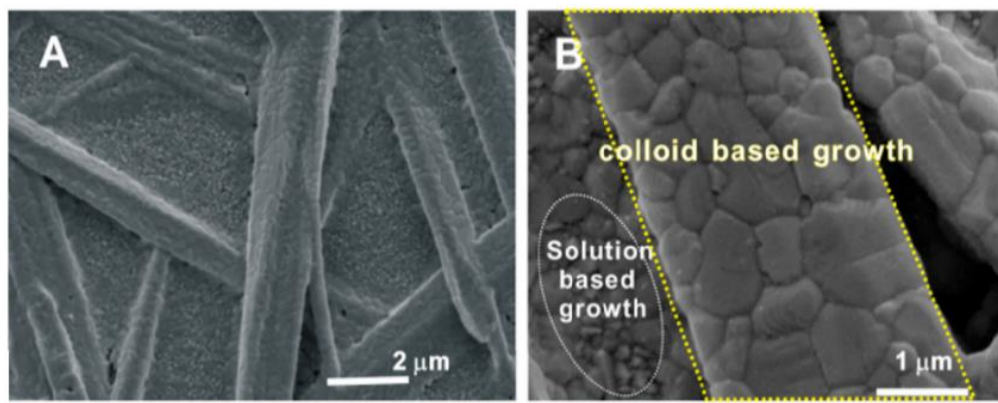


Figure 2. 4: SEM images of MAPbI₃ perovskite thin films, showing both solution based growth and colloidal based growth with orientated attachment.⁴⁵

Figure 2.4 shows the film morphology for solution processed MAPbI₃ perovskite film. The observation of large dendrites in the crystalline film can be seen in these images. This observation sparked interest in studying and understanding the nucleation and crystallization mechanisms in more detail. Through further study of hybrid perovskites, it was learned that the precursor solutions consist of colloids and intermediate compounds. The colloids were found to orientate preferentially in order to reduce the overall energy of the system. In solution, a soft framework of the inorganic species is developed, surrounded by the bulky organic ions in solution. When the organic solute is used in excess, this framework is made of smaller inorganic colloids, resulting in more uniform films.⁴⁵⁻⁴⁷

As mentioned, the use of excess organic precursor has been shown to assist in the formation of uniform perovskite films. The excess organic salt precursor, like MAI, can be added to an alternative lead source, like Pb(Ac). This combination forms an intermediate MAAc, which is volatile and can be driven off in the annealing process. When an organic excess molar ratio of 3 is used, additional benefits of more crystallinity and larger grains sizes are achieved. Limiting the formation of PbI₂ seems to be an additional benefit of the excess organic salt.³⁰

The use of chloride additives in the one-step preparation of high quality perovskite thin films has been demonstrated as beneficial to formation of quality uniform grains. Some studies suggest that the MACl additive participates in the crystallization by effectively slowing the kinetics of the reaction down through the creation of intermediate compounds in solution. The additive acts like a glue which helps hold the precursors in place while retarding the crystallization. The chloride is driven out through the annealing period, possibly by sublimation of the MACl. Other volatile additives like HCl or NH₄Cl have been shown to be effective in enhancing the morphology of perovskite films.³⁰

Use of an anti-solvent (AS) has a positive effect on the fabrication of large-grain uniform perovskite films in some cases. The AS can be dripped onto the spin coated film before crystallization and after a critical delay period. The solution is in a state of supersaturation when the AS is added resulting in homogeneous nucleation. After a subsequent annealing step the resultant film morphology is observed. A solvent annealing process is shown to be more beneficial to planar device architectures rather than devices with a mesoporous substrate. Thermal annealing seems to be more optimal for devices based on the n-type PSC utilizing a mesoporous layer.⁴⁸

Due to the importance of film morphology in the final efficiency of perovskite solar cells, there is a continued push to work towards a better understanding of the deposition process. As new compositions and processing routes are introduced in the field, there will likely be reference to early works that provided understanding of the nucleation and crystal growth mechanisms of metal halide perovskite solar materials.

A typical synthesis route of lead halide solar cells involves spin coating and annealing the film onto a glass slide with a conductive oxide layer and a subsequent layer of a wide bandgap metal oxide, i.e. TiO_2 . The wide band gap oxide has been shown to work as a mesoporous or planar layer in high efficiency devices.⁴⁹

For solution processing, a typical precursor solution is prepared by dissolving a halide salt (i.e. PbI_2 , SnI_2) in a 4:1 v/v ratio of DMF/DMSO. Concentrations of 1.5 moles per liter are typical for stock precursor solutions. Moderate heat is applied to fully dissolve the salt into solution until they are clear. These stock solutions are sealed and stored in a nitrogen or argon filled gloveboxes and trace moisture is maintained below 1 ppm.⁴³

Synthesis routes can also include the use of anti-solvent (AS) drenching after the precursor solution has been deposited. In these cases the AS drenching induces the crystallization of intermediate phases which are believed to act as seeds to crystallization, resulting in a uniform thin film. It is also possible to create films by use of AS alone, eliminating the need for a thermal annealing step.

A perovskite film can be deposited directly on a glass slide for material characterization or deposited on a charge carrier transport layer to be built into a working PV device.

Depending on the specific architecture of solar cell, processing conditions can vary. A

typical annealing is carried out on a preheated hotplate, ranging in temperature from 80°C to 200°C. Solution-based processing of films was chosen for the current work due to speed of processing and relatively low equipment and material cost.

2.2.2 Vapor Deposition

Efficient perovskite solar cells have been shown to be possible without the mesoporous structures inherited from the DSSC synthesis routes by utilizing a compact layer architecture. Vapor deposition can then be used to deposit the perovskite film to achieve high performance devices. Perovskite films synthesized by dual-source vapor deposition show increased uniformity and create higher efficiency cells when compared to the same device where the perovskite layer was deposited by solution-based methods.²⁴

2.2.3 Single Crystal Growth

As new perovskite semiconductor formulations are explored, single crystal growth has become a common method for crystallization for material characterization purposes. A common method involves the dissolution of a precursor salt into an acid that corresponds to the target halide of the final crystal, i.e. HI, HBr and HCl. A supersaturation is made at an elevated temperature around 120 °C. The solution is held for several hours and then slowly cooled, undisturbed, at a rate of around 1-2°C/hr. Crystals precipitate out of solution and can be harvested, or placed in a fresh solution as seed crystals and grown to larger sizes.^{50, 51, 52}

2.2.4 Inverse Solubility Crystal Growth

In the early years of perovskite solar cell research, it was observed that certain perovskite systems exhibit a unique inverse solubility. When a solution of salts is heated above a

certain temperature, the solubility decreases and single crystals begin to form out of solution. This process is much faster than the typical crystallization upon cooling as mentioned above. The solvents used to perform these reverse crystallizations are chosen for each salt, where iodide salts in GBL have been shown to work well. For bromide salts, the more common solvent, DMF is used.⁵³

2.2.5 Mechanochemistry

Perovskite crystals can be formed by simply mixing the halide salts together and grinding them in a mortar and pestle. This very simple method does not typically yield a homogeneous mixture. However, a more aggressive mixing by ball milling has shown promise as synthesis route of perovskite semiconductor materials. Mechanochemistry has the advantage of being environmentally clean and more energy efficient. Devices based of this synthesis method have been shown to outperform their solution processed analogs.⁵⁴

2.3 Perovskite Film Characterization

Perovskite light-absorbing films are often characterized on their own to help predict performance and explore new compositions and processing methods.

UV/Vis absorption spectroscopy is used to estimate the bandgap energy of the absorbing films and can also give qualitative information about the nature of the bandgap, i.e. direct or indirect. A direct bandgap is favorable for more efficient power conversion. With an indirect bandgap material, energy is needed to change momentum in addition to exciting a free electron over the bandgap energy. The same incident light results in less current generation, reducing the overall efficiency of the solar cell.

Standard characterization techniques utilized by researchers in the area of perovskite solar cells include X-Ray diffraction (XRD) and scanning electron microscopy (SEM). XRD is utilized to quantify the crystallinity of the perovskite as well as the experimental stoichiometry of the crystal and any intermediates and/or recrystallized precursor. XRD patterns provide insights into intermediate phases that exist during and after crystallization, which helps to better understand crystallization mechanisms. The utilization of SEM-EDX has been used to characterize degradation mechanisms in combination with XRD and Raman spectroscopy.⁵⁵

SEM images can be useful in investigating and measuring the morphology and thicknesses of thin films and nano-structured perovskites. Grain size, shape and morphological features like pinholes are of interest due to their effects on solar cell performance.

Photoluminescence (PL) is a characterization method that is useful in understanding the way the hybrid perovskite functions as a light absorber material. PL is the measure of the light that is emitted when an electron and hole recombine in a material after the absorption of photons. The use of a technique called PL quenching has been shown to quantify the diffusion length of charge carriers, the charge carrier lifetimes, and their diffusion rates in perovskite materials.⁵⁶ This is done by fabricating two thin films of perovskite, one with a hole conducting or “quenching” layer and one without a quenching layer. Carrier diffusion lengths and lifetimes determine the probability of a charge carrier reaching the device electrodes, relating directly to the efficiencies of solar cells. By modeling the PL decay with a diffusion equation the properties of the charge carriers can be derived.

Photoluminescence measurements are also used to estimate bandgap energy and quality of films based on relative non-radiative recombination measurements. The non-radiative component of recombination can be related to the quality of a series of films made by varying preparation techniques or annealing parameters.

Due to the infancy of the metal halide perovskite field, several specialized characterization techniques have been employed to gain new insights into this emerging technology. Most of these techniques are utilized to better understand the underlying photophysics and chemistry involved in the fabrication, operation and degradation of the perovskite absorbing layer. In-situ GIXRD and in-situ UV-Vis Spectroscopy have been found useful in better understanding the degradation mechanism of the hybrid perovskite in the presence of water. A combination of electroluminescence and photovoltaic external quantum efficiency measurements has also been used in predicting the open circuit voltage of different variations of metal halide perovskite cells.

2.4 J-V Performance of the PSC Device

Characterization of hybrid perovskite solar cells is similar to other photovoltaics, where a primary figure of merit is power conversion efficiency (PCE). In order to derive PCE, a current density-voltage (J-V) curve is plotted under a standard illumination, typically AM 1.5 at room temperature. When the current density and voltage are plotted together the short circuit current density (J_{sc}) and the open circuit voltage (V_{oc}) are determined. A maximum power (P_{max}) and fill factor (FF) can be calculated by Equation 15.

$$FF = \frac{P_{max}}{J_{sc} \times V_{oc}} \quad (15)$$

The power conversion efficiency can be determined from the P_{max} and the power input which comes from the standard illumination conditions. The efficiency is determined by Equation 16.

$$PCE = \eta = \frac{P_{max}}{P_{input}} \quad (16)$$

While characterizing perovskite solar cells, an anomalous hysteresis is observed in its J-V curve. In the reverse scan from the open circuit to the short circuit, an increased efficiency is observed. When scanning forward from the short circuit to the open circuit condition, the efficiency is decreased for the same device. Increases in scan rate tend to exacerbate the deviation from the device's mean efficiency.⁵⁷

While the origin of hysteresis in perovskites is still debated, a few common theories are noted. A capacitive current is observed when sweeping between forward and reverse bias. A non-steady photocurrent from this capacitive current effect causes polarity at the interface of the perovskite film, having an effect on hysteresis. The interfacial polarization and the related dielectric constant may be the origin of the observable capacitive current effect.³⁰

Trap states created by the grain boundaries and defects in the perovskite films may also play a role in the hysteresis observed. The trapping and de-trapping of charge carriers is thought to reduce the charge extraction efficiency. The proposed mechanism, under forward bias, is that a depletion region is created at each perovskite/selective layer interface resulting in lower extraction efficiencies. Under the reverse bias, this effect is thought to be minimized, resulting in the higher efficiencies being observed. Due to the

short time scales of trapping and de-trapping processes compared to the time scale of the hysteresis observed, this mechanism is thought to play a minor role in perovskite hysteresis.⁵⁸

Band bending caused by ion migration to the interfaces can affect the steady state photocurrent and play a role in hysteresis. In MAPbI₃, the formation energies of iodine vacancies and interstitial defects are both 0.08 eV. This is relatively low compared to the formation energies of MA vacancies and Pb vacancies, which are 0.46 eV and 0.80 eV, respectively. With the relative ease of iodine ion migration under an applied bias, this mechanism is suspected as a cause of hysteresis by altering band states in the crystal.⁵⁹

Another band bending mechanism that has been proposed involves the potential presence of an organic dipole or lattice polarization, resulting in hysteresis similar to that seen in ferroelectric materials. This theory has been challenged due to the mismatch of frequency in perovskites compared to ferroelectrics as well as observation of fully disordered organic dipole distributions observed by NMR. Grain sizes of larger millimeter size have been shown to produce hysteresis-free J-V curves, while the use of fullerenes and fullerene-based materials and charge transport layers has shown to significantly reduce the severity of hysteresis.³⁰

2.5 Stability

Most PSCs are not inherently stable under normal conditions and several challenges exist that must be address before commercial success can be achieved. The hybrid perovskite material is sensitive to water, temperature, oxygen, UV light and diffusion of species

from carrier transport materials. Better understanding the mechanisms of degradation from environmental factors will help design better processes and devices.

The degradation by water is one of the most critical challenges since humidity and water are especially difficult to avoid in real world applications. Another major factor when dealing with toxic elements, like Pb, is that the degradation by water may lead to contamination of water sources. The mechanism is revealed by in-situ UV/Vis spectroscopy and XRD measurements.⁵⁵ Kelly showed that upon hydration of MAPbI₃, leads to an intermediate hydrated species (CH₃NH₃)₄PbI₆ · 2H₂O + PbI₂ by a reversible reaction. If the perovskite was not re-hydrated, the degradation would continue to generate additional H₂O, PbI₂, CH₃NH₃ (MA) and HI as degradation products.

Elevated temperatures are commonly used to crystalline perovskite films through thermal annealing, but also play a role in device stability fabrication. Wang showed how temperature affected the efficiency of a MAPbI₃ device through varying temperatures.³⁴ A phase transition from tetragonal to orthorhombic has a drastic and negative effect on device performance below 240 K as it approaches the Curie temperature of 160 K. In higher temperature ranges, the MAPbI₃ device reaches a maximum efficiency 16% around 300 K, which more gradually decreases to about 9% at 360 K. This temperature region corresponds to the gradual transition from tetragonal to cubic around 327 K.

3. Fabrication and Characterization of Pb-free Halide Perovskites

3.1 Background

Awareness of toxicity in electronic devices has increased in recent years, especially with regards to end-of-life design and disposal of electronic waste. As we enter into an age where we are increasingly able to develop new functional materials, we should have the foresight to work toward developing devices that can be easily and safely disposed of after their usable life. Toxicity of the ionic lead contained in all high-performing perovskite solar cells poses a biological hazard. If these cells are deployed and subsequently destroyed or disposed of improperly, contamination of the surrounding environment would be likely.

These facts lead to the primary motivation for this research. Searching for a highly efficient perovskite solar cell without the use of Pb. One of the properties of lead-based perovskites that makes it work so well is its near optimal direct bandgap, 1.4-1.5 eV.³⁰ While searching for a non-toxic halide perovskite material, it would be desirable to find a direct band gap close to 1.34 eV which is also solution processed and stable over time.

Tin is a natural choice as an alternative system to lead as a fellow group-14 element with a similar valence electron configuration. In addition, the ionic radius of Sn²⁺ is only 7.5% smaller than Pb²⁺ allowing the formation of the ABX₃ structure, analogous to the lead halide perovskites.

Tin-based perovskites can be processed with a variety of procedures, but some common trends include the assistance of solvent engineering and the addition of SnF₂.⁶⁰ A solvent mixture of DMF and DMSO is typically employed. The DMSO is used as both a solvent and a mediator in the formation of intermediate phases that result in more uniform perovskite films. The addition of SnF₂ has been proven successful in inhibiting the oxidation of the Sn²⁺ to Sn⁴⁺ during the deposition process. More recent works have shown successful techniques to create a more uniform perovskite thin film by controlling the local atmosphere and evaporation rates of the solution during the annealing step.⁶¹

FASnI₃ has been fabricated with efficiencies around 6%.⁶² The direct bandgap of FASnI₃ is measured to be 1.41 eV which aligns with its relatively high performance. The largest drawback of the tin-based halide perovskite is the desire for the Sn²⁺ to return to its oxidation state of Sn⁴⁺. For this reason all devices have required inert environment for fabrication and have faced challenges regarding long term stability.

Alternatively, moving from group-14 Pb to group-15 on the periodic tables gives us bismuth, Bi. Due to the difference in valance charge, bismuth does not directing form a 3D perovskite structure like MAPbI₃. Instead, lower dimensional perovskites are formed where bismuth halide octahedrals are arrange in 0D bioctahedrals, 1D chains or 2D layers.^{63, 64} These materials tend to have higher bandgaps and higher charge carrier recombination rates, but are still investigated for solar applications.⁶⁵

To make trivalent Bi³⁺ fit into a 3D perovskite structure, one can combine a monovalent metal to create a double perovskite structure. Most double perovskites that have been synthesized tend to have higher, indirect bandgaps, which make them less suitable for

solar application. Theoretically, double perovskites based on the larger iodide halide should have lower and more direct bandgaps, but these materials have been difficult to realize in the laboratory.⁶⁶

Double perovskites of the formula, $A_2BB'X_6$ have received a good deal of attention due to the myriad of combinations that can be formulated.^{51, 67-70} In order to achieve charge balance, the B atom is chosen to be monovalent and the B' atom is trivalent, in a 1:1 stoichiometric ratio to preserve charge balance over the entire crystal. Many studies have been driven by first-principles calculations of electronic properties to help direct researchers toward promising materials. Computational materials science methods can screen for potential candidates using criteria including theoretical bandgap energy, bandgap positions, perovskite crystal structure stability, toxicity and effective charge carrier masses. High-throughput screening allows for rapid disqualification of materials that would be less suitable for use as solar absorbing materials. The experimental work in this thesis was guided by previously published computational results in **Table 3.1**.⁷¹

Table 3. 1: Reference computed theoretical electronic band structure for possible double perovskites of the $A_2BB'I_6$ formula where $A = FA, MA, Cs$ and $B/B' = Bi, Sb, In,$ and Ag . Computation is based on spin-orbit hybrid HSE functional.⁷¹

Metal Ions	Target Compound	Theoretical Band Gap (eV)	Nature of Bandgap	Forms Perovskite
Bi + In	FA_2BiInI_6	1.19	Direct	Yes
	MA_2BiInI_6	0.88	Direct	Yes
	Cs_2BiInI_6	N/A	Metallic	Yes
Sb + In	FA_2SbInI_6	N/A	Metallic	Yes
	MA_2SbInI_6	1.01	Direct	Yes
	Cs_2SbInI_6	N/A	Metallic	Yes
Bi + Ag	FA_2BiAgI_6	1.63	Indirect	Yes
	MA_2BiAgI_6	2.09	Indirect	Yes
	Cs_2BiAgI_6	N/A	N/A	N/A
Sb + Ag	FA_2SbAgI_6	1.29	Indirect	Yes
	MA_2SbAgI_6	1.89	Indirect	Yes
	Cs_2SbAgI_6	N/A	Metallic	Yes

While lower bandgaps have been predicted by first-principle calculations of $A_2BB'X_6$ perovskites, most compounds utilize iodine in the X position. Three-dimensional double perovskites where $X = I^{-1}$ have been challenging for researchers to crystalize.^{66,72} The lower dimensional Bi^{3+} -based materials based on the formula $A_3Bi_2I_9$ have not been realized in a 3D perovskite. Higher order has been shown with smaller A site atoms, $A = K$ or Rb , which crystalize as a 2D polymorph, demonstrated by Lehner.⁷³

3.2 Low-Toxicity Perovskite Film Fabrication

3.2.1 Organic FAI Synthesis

Formamidine iodide (FAI) was synthesized by adding 0.94 g of formamidine acetate powder, 99% (Alfa Aesar) to a ceramic crucible, then subsequently adding 2.95 g of hydriodic acid, 57% w/w aq. soln., stabilized with 1.5% hypophosphorous acid (Alfa Aesar). The mixture was placed on a hotplate with a magnetic stir bar and was covered. The hotplate was heated to 50°C and moderately stirred for 10 minutes. Powder was completely dissolved.

The solution was then placed in a vacuum oven, a vacuum was drawn and the oven was heated to 100°C and left for 2 ½ hours. A solid white-yellow precipitate was left after evaporation of the liquid. Using a Buchner funnel and filter flask with a paper filter, the solid was washed three times with diethyl ether, HPLC grade, 99% stabilized with ethanol (Alfa Aesar). The retained solid was progressively whiter through the washing process, the supernatant was a red-yellow color. The retentate was collected and placed in a glass beaker with a magnetic stirring rod and placed on a hotplate and covered. The hotplate was heated to 80°C and absolute ethanol was added dropwise while stirring while watching the solid dissolve. In order to ensure a supersaturation, the last small amount of solid was left in the solution and ethanol addition was stopped. The solution was left to stir for 10 minutes. The stirring was stopped and the solution was allowed to settle. The clear-yellow solution was decanted into a new glass vial, avoiding solids to enter the glass vial. The vial was capped and immediately placed in a laboratory refrigerator at approximately 4°C and left to recrystallize for 24 hours. A white, needle-like precipitate crystallized out of the solution. The precipitate was washed once with ethanol and placed

in a vacuum oven for 24 hours at 50°C. The FAI was then moved to the Argon filled glove box for use and storage.

3.2.2 FAPbI₃ Precursor

A 1M solution of FAI in dimethyl sulfoxide (DMSO), anhydrous, 99.9% (Sigma-Aldrich) and a 1M solution of lead (II) iodide, ultra dry, 99.999% (Alfa Aesar) in DMSO were prepared in an argon-filled glove box. The solutions were stirred for 20 minutes at 60°C and solutions were visually transparent. A molar ratio of 3:1 was made by combining volumes of the FAI precursor and PbI₂ precursor, then mixing them with stirring and heated to 60°C for approximately 5 minutes. The three-fold excess of organic precursor was used to achieve improved film crystallization as demonstrated by previous works.

3.2.3 FASnI₃ Precursor

A 1M solution of tin (II) iodide, anhydrous, 99.99% (Sigma-Aldrich) in DMSO and a 0.2M solution of tin (II) fluoride, 99% (Sigma-Aldrich) in DMSO were prepared in an argon-filled glove box. The SnI₂ and SnF₂ solutions were mixed at equal volumes to maintain the stoichiometric ratio of 4:1. The organic FAI precursor was mixed at a 3:1 molar ratio relative to the SnI₂ precursor. The mixture was stirred and heated to 60°C for 5 minutes. The precursor was stored in the argon-filled glovebox.

3.2.4 Lead-free Precursors

Driven by recently published first-principle studies, the following B/B' site metals were chosen, Bi⁺³, Sb⁺³, In⁺¹ and Ag⁺¹. Inorganic precursors were composed of iodide salts of the previously stated metals and were prepared as described below, at room temperature and in an argon-filled glovebox. All iodide salts were opened and stored in an

inert environment, to avoid degradation. A 1.5M solution of FAI was prepared in 100% DMF at room temperature in an argon-filled glovebox. Films were drop-cast onto microscope slides and transported as quickly as possible to the UV/Vis spectrometer, which was in ambient air conditions.

3.2.4.1 CsI

Cesium (I) iodide, 99.9% (Sigma-Aldrich) was dissolved in 100% DMSO under stirring and on a hotplate at 60°C. Solution was transparent and clear in color. The precursor was stored in glovebox and used within 2 months of preparation.

3.2.4.2 BiI₃

Bismuth (III) iodide, Puratronic®, 99.999% (Alfa Aesar) was dissolved in DMF:DMSO at a volumetric ratio of 7:3. Bismuth iodide crystals were ground in a mortar and pestle and weighed to create a 1.5M solution. The mixture was left stirring for 1 hour at 80°C.

3.2.4.3 SbI₃

Antimony (III) iodide, ultradry, 99.999% (Alfa Aesar) was dissolved in DMF:DMSO at a volumetric ratio of 7:3 to create a 1.5M solution. Antimony iodide beads were ground in a mortar and pestle. The mixture was stirred for 1 hour at 80°C.

3.2.4.4 AgI

Silver iodide, 99.9% (Alfa Aesar) was dissolved in 100% DMF to create a 1.5M solution. Solution was left stirring for 20 minutes at 60°C.

3.2.4.5 InI

Indium (I) iodide, ultradry, 99.998% (Alfa Aesar) was dissolved in 100% DMSO to create a 1.5M solution. Indium iodide beads were ground in a mortar and pestle.

Solution was left stirring for 1 hour at 60°C.

3.3 Perovskite Film Characterization

3.3.1 UV/Vis Spectroscopy

Electronic band structures can be probed by absorption spectroscopy. In this work a Varian Cary 50 Scan Ultraviolet-Visible Spectrophotometer using a Cary Solid Sample Holder was employed. Ultraviolet-Visible (UV-Vis) spectroscopy works by splitting a light source and directing specific and wavelengths of light at the sample holder. The intensity of the light before the sample holder (I_0) is compared to the intensity of the light that reaches a detector on the opposite side of the sample (I). Transmission (T) and absorbance (A) are defined by the following equations.⁷⁴

$$T = \frac{I}{I_0} \quad (17)$$

$$A = \log_{10} \frac{I_0}{I} \quad (18)$$

Using a Tauc Plot, a bandgap estimation can be derived. The photon energy vs. $(Ah\nu)^n$ were plotted, where n is related to the nature of the bandgap, h is Plank's constant and ν is the frequency of the photons. For the purposes of bandgap estimation, $n = 2$. A linear fit is made on the higher slope section on one side of the transition of the Tauc plot. Next a second line is drawn, fitting a linear section at lower photon energy section of the transition. The photon energy at the intersection of these two lines is taken as the

estimated bandgap energy. It should be noted that bandgap estimations in this work are used to probe candidate materials for further research using a comparative approach to similar materials, with a focus on solar cell application and are not to be taken as the actual bandgap.

3.3.2 X-Ray Diffraction

Crystalline characteristics of solids can be understood by use of X-Ray diffraction (XRD). XRD patterns are plots of detected intensity of X-Rays that were diffracted by the sample being measured. Diffraction peaks occur from scattered light from atoms that are periodically arranged with long range order, resulting in constructive interference at specific angles. Diffraction patterns contain information about the crystallographic arrangement and spacing of atoms in a crystalline material. The diffraction angle, θ , and the physical spacing of a given crystallographic plane, d_{hkl} , is related by Bragg's law, where λ is the wavelength of the X-Ray source.⁷⁵

$$\lambda = 2d_{hkl} \sin \theta \quad (19)$$

In the current work, XRD patterns were measured by chromium radiation from a Bruker D8 Discover diffractometer utilizing a 1-dimensional Linxeye detector with a parallel beam geometry. The sample was drop cast and annealed on an amorphous glass slide and mounted in the diffractometer. The source was operated at 30 kV and 45 mA with a 1 mm collimator. Patterns were taken from 2θ angles $10^\circ - 165^\circ$ with a step size of 0.075° and at a rate of 2 seconds per step.

3.4 Results and Discussion

3.4.1 Lead-Tin Mixed Films

3.4.1.1 FAPbI₃

The FAPbI₃ precursor was drop cast onto a glass slide that was preheated to 170°C. The film was annealed for 20 minutes and the solution turned from a transparent yellow color to a dark film, which agrees with accounts published in literature. This exercise was done to replicate the work done in the literature and to setup best practices in film synthesis.

3.4.1.2 FASnI₃

The FASnI₃ precursor was drop-cast onto a glass slide that was preheated to 100°C. The film was annealed for 20 minutes. Samples were placed in a sample holder while in the argon-filled glovebox. The sample holder was opened only after transporting the sample to the UV-Vis spectrophotometer. This period could take up to an hour and noticeable color change of the films was observed. UV-Vis spectra were taken and noisy signal was observed at higher wavelengths, relating to relatively low known bandgaps of FASnI₃, ~1.4 eV. It is seen in the UV-Vis spectrum, in the Appendix, that there is a possible bandgap around 1.2 eV. The maximum wavelength was 1100 nm, which is a known limitation of the UV-Vis spectrophotometer used in this work. Within minutes of this measurement, repeat measurements show that this event in the spectrum disappears, likely related to the oxidation and degradation of the film.

3.4.1.3 FA₂PbSnI₆

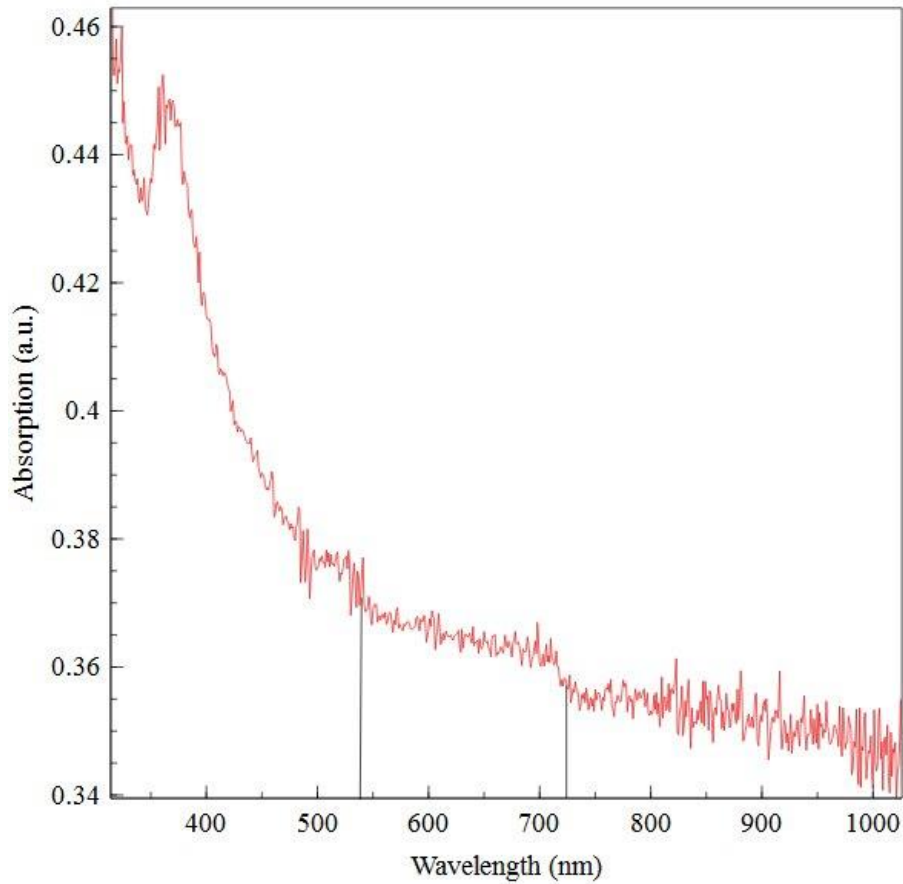


Figure 3. 1: UV-Vis Spectrum of combination of FAI, SnI₂ and PbI₂ in a 3:1:1 stoichiometric ratio. Vertical lines indicate an observed increase in absorption, indicating an electronic bandgap.

The mixed lead-tin system was used as a starting point to attempt to match results by previously reported results which demonstrate a bandgap tuning effect.⁷⁶ Several films were created in this series and there were challenges relating to decomposition of the Sn²⁺ to Sn⁴⁺. This was known from previous work and was seen in the measurement of the UV-Vis spectrum, with a large increase in absorption around 300 nm, which is likely due to the presence of SnO₄. UV-Vis spectrum show a bandgap observed around 720 nm,

corresponding to 1.7 eV. A second phase was observed in the film with a bandgap at approximately 530 nm, corresponding to 2.3 eV (**Figure 3.1**).

3.4.2 Mixed Metal (In, Sb and Bi) films

Crystallization of $\text{FA}_2\text{BiInI}_6$ and $\text{FA}_2\text{SbInI}_6$ was attempted by combination of FAI, SbI_3 or BiI_3 , and InI precursors combined in a 3:1:1 molar ratio and annealing at 100°C under argon for 20 minutes. Samples were stored under argon and removed less than one hour before exposure to air for UV-Vis measurement. The excess organic cation has been shown to help arrange the MI_6 octahedrals immediately before crystallization occurs, resulting in a more uniform polycrystalline thin film.³⁰ The antimony and indium combination did not show an estimated bandgap in the target range, below 2.5 eV (see Appendix).

The bismuth and indium combination showed a bandgap around 2.2 eV. A lower bandgap is also observed, likely due to residual, unreacted BiI_3 precursor. BiI_3 has a relatively narrow bandgap of 1.7 eV and it is seen in the spectrum in **Figure 3. 2**.

Four films were annealed with 3:1:1 ratios of FAI, BiI_3 and InI at different temperatures and varied times as listed in **Table 3.2**. As the temperature of annealing was increased, it was seen visually that the film went from a light red color, to a dark red color and finally to a black color. Lower temperature and longer annealing time resulted in a film with little residual BiI_3 precursor.

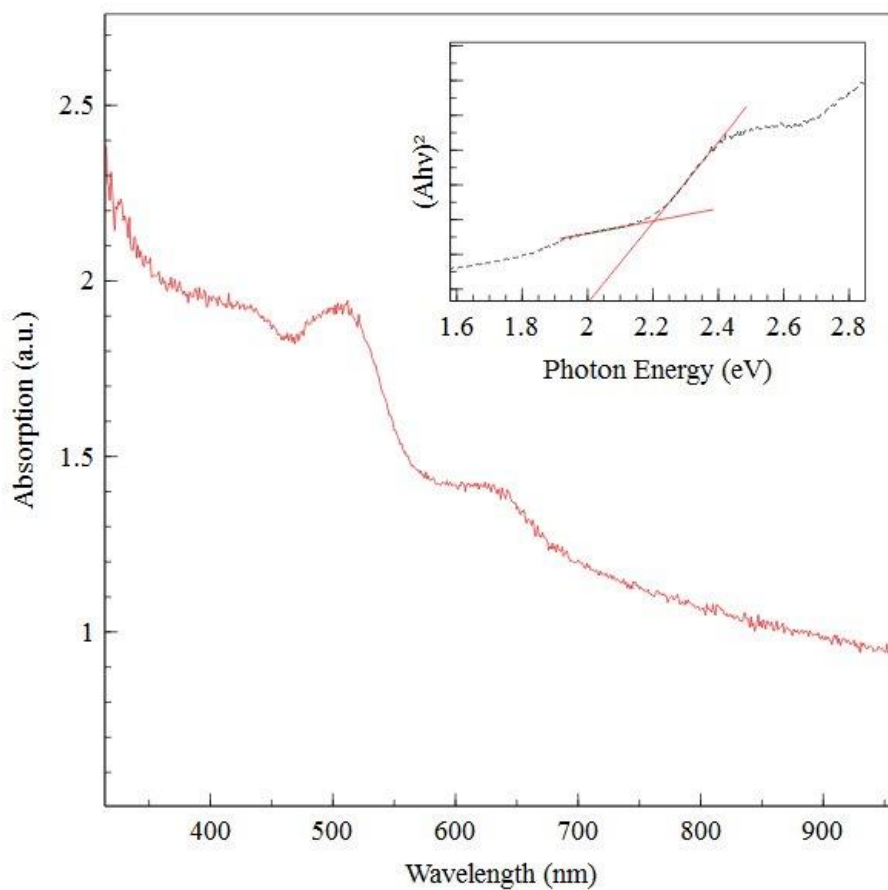


Figure 3. 2: UV-Vis Absorption and Tauc Plot for combination of FAI, BiI₃ and InI precursors. Bandgap estimation is intercept of fit line (red) in inset Tauc Plot.

Table 3. 2: Annealing effects on estimated bandgap and detection of residual precursor phase.

Annealing Time (min)	Maximum Temp (°C)	Appearance/Color	Estimated Bandgap (eV)	BiI ₃ bandgap
10	75	Light red	2.25	No
15	90	Dark red	2.15	No
20	125	Black/red	2.00	Yes
1	150	Black	2.05	Yes

XRD patterns of this material, seen in **Figure 3.3**, did not match theoretical XRD patterns for FA₂BiInI₆. The ~2 eV bandgap estimated by UV-Vis is also much larger than the

theoretical $\text{FA}_2\text{BiInI}_6$ bandgap of 1.19 eV, **Table 3.1**. Further investigation of this result show a 0D perovskite of $\text{FA}_3\text{Bi}_2\text{I}_9$ was likely formed by the described process. The XRD peaks correlate well to $\text{FA}_3\text{Bi}_2\text{I}_9$ peaks from literature and the bandgap also corresponds to the reported value of this material.⁷³ The 0D $\text{A}_3\text{Bi}_2\text{I}_9$ crystal consists of complex anions of two face-sharing octahedrals and of the formula $\text{Bi}_2\text{I}_9^{3-}$. The metal halide clusters are surrounded by A-site cations.

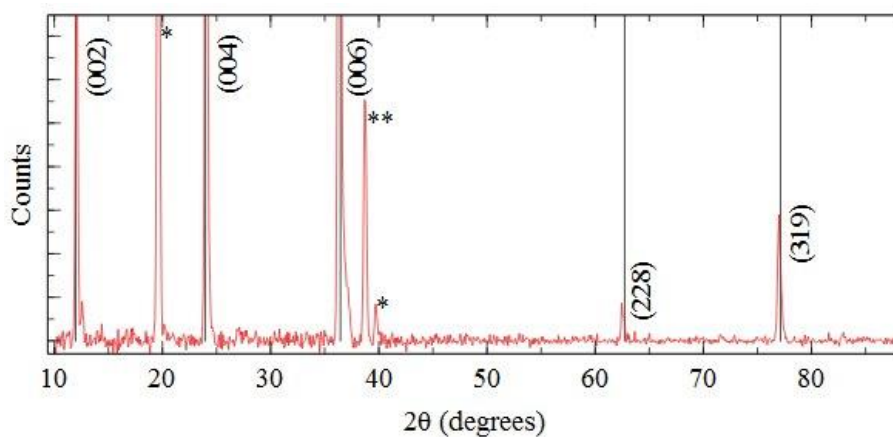


Figure 3. 3: XRD pattern of combination of FAI, BiI_3 and InI with reference peaks labeled by black vertical lines. Peaks labeled with an asterisks (*) are attributed to BiI_3 based on reference peaks in Appendix. The peak labeled (**) is unidentified.

3.4.3 Tin-alloyed FA Bismuth-Indium film

A series of films were made by combination of FAI, BiI_3 , InI precursors with the incremental addition of $\text{SnI}_2/0.2\text{SnF}_2$ precursor. Films were processed by drop casting and annealing for 15 minutes at 90°C . UV-Vis spectra were measured and bandgap estimations were made. A slight trend of increased bandgap ranging from 2.0 eV to 2.25 eV can be seen in **Figure 3.4**. While the bandgap value increases, it is observed that the

strength of the transition decreases in the series. UV-Vis spectra are displayed in the Appendix for this series.

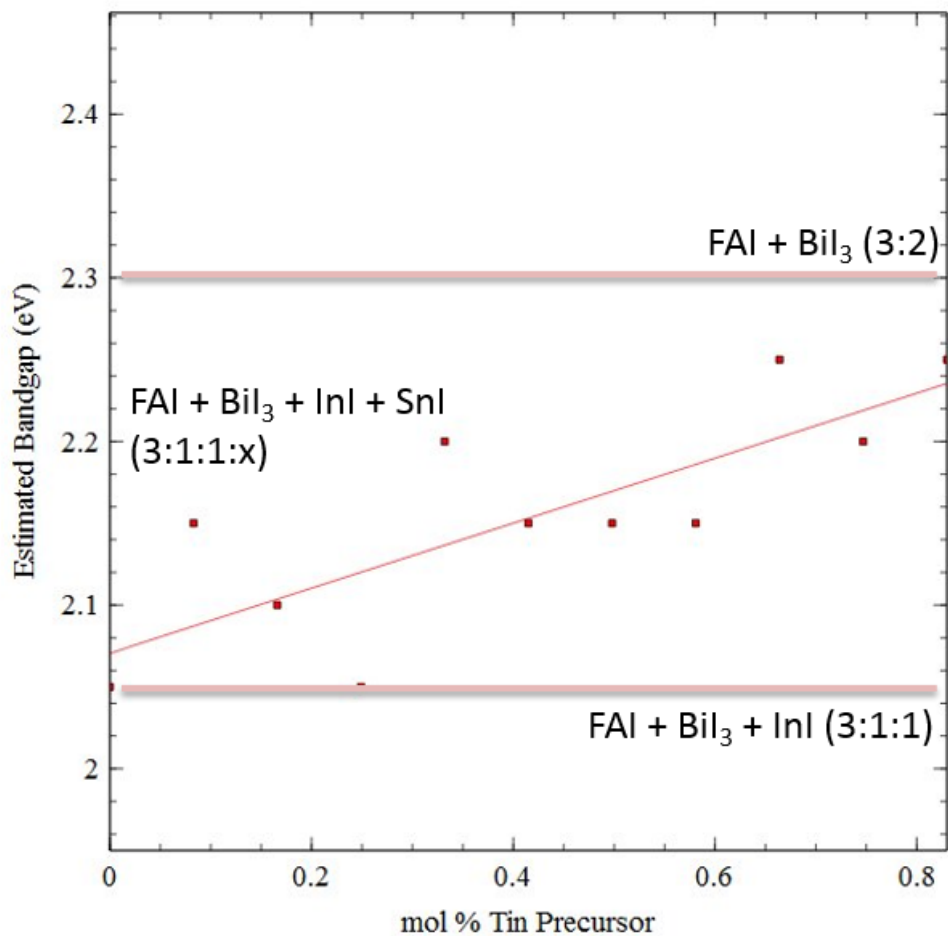


Figure 3. 4: Plot of Estimated Bandgap vs. mol % of Tin precursor in films synthesized by combination of FAI, BiI₃ and InI.

3.4.4 Cesium Bismuth-Indium Perovskite

Cesium can be used as the A-site cation to probe the resultant crystal that forms. A combination of CsI, BiI₃ and InI precursors was combined in a 2:1:1 stoichiometric ratio.

Figure 3.5 shows the UV-Vis spectrum and a Tauc plot with an estimated bandgap of 2.25 eV. The XRD pattern is matched with Cs₃Bi₂I₉ peaks from literature and show good agreement in **Figure 3.6**.⁷³

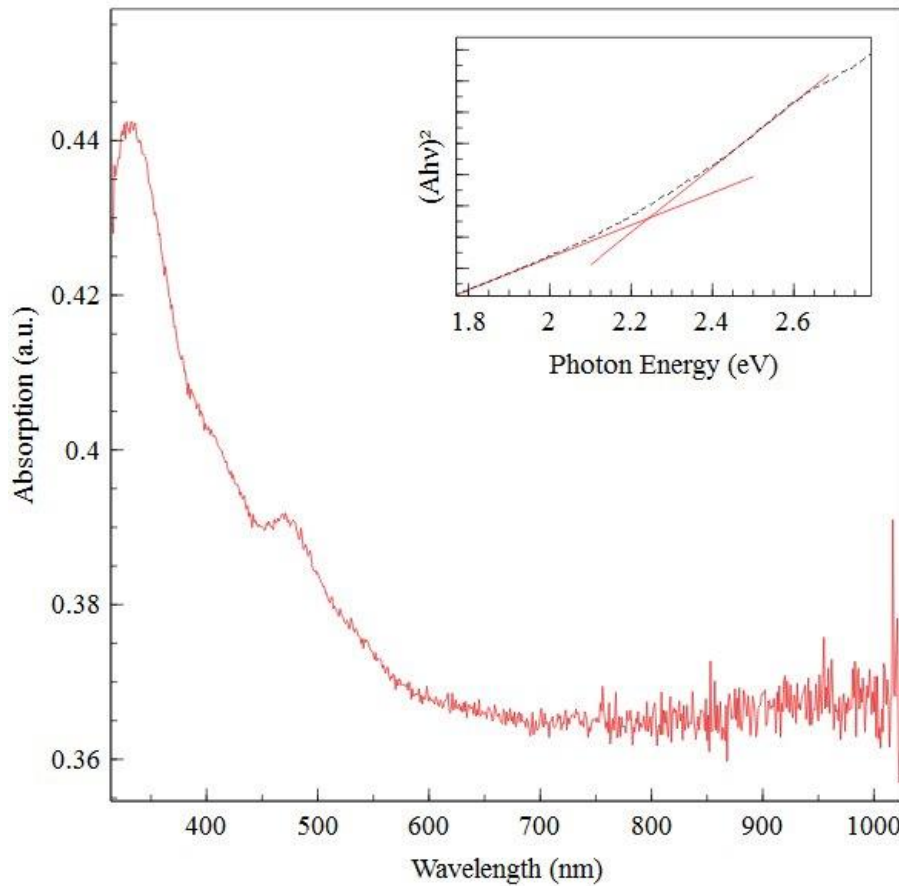


Figure 3. 5: UV-Vis spectrum for combination of CsI, BiI₃ and InI with estimated bandgap at 2.25 eV.

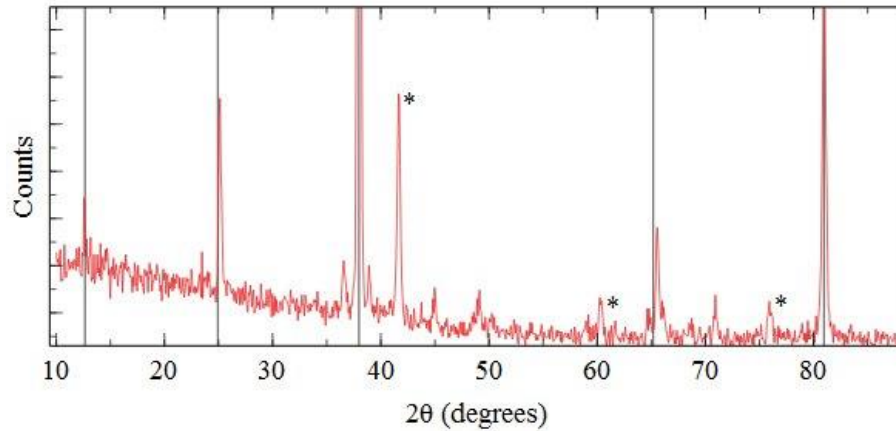


Figure 3. 6: XRD pattern for combination of CsI, BiI₃ and InI with reference peaks of Cs₃Bi₂I₉ as black vertical lines. Peaks labeled with an asterisks (*) are attributed to CsI based on reference peaks in Appendix.

3.4.5 Low-Dimensional Bismuth Perovskite

3.4.5.1 Cs₃Bi₂I₉

CsI and BiI₃ were combined, drop-cast and annealed to synthesize films for UV-Vis and XRD characterization. Similar bandgaps and XRD patterns (see **Figure 3.7** and **Figure 3.8**) were observed and compared to the previously synthesized films using InI precursor. XRD patterns are matched to reference peaks of Cs₃Bi₂I₉ with good agreement.

3.4.5.2 FA₃Bi₂I₉

FAI and BiI₃ were combined, drop-cast and annealed to synthesize thin films for characterization. UV-Vis indicates several bandgaps in the material, including a 2.3 eV estimated bandgap which most likely is due to the presence of FA₃Bi₂I₉. The estimated bandgap is slightly higher than the bandgap from the previous synthesis using InI precursor. This indicates there may be a depression of the bandgap with the presence of In in the film. The XRD pattern is quite different from the previous film, indicating other

phases were formed. This fact is also highlighted by the presence of multiple absorption transitions in the UV-Vis spectrum.

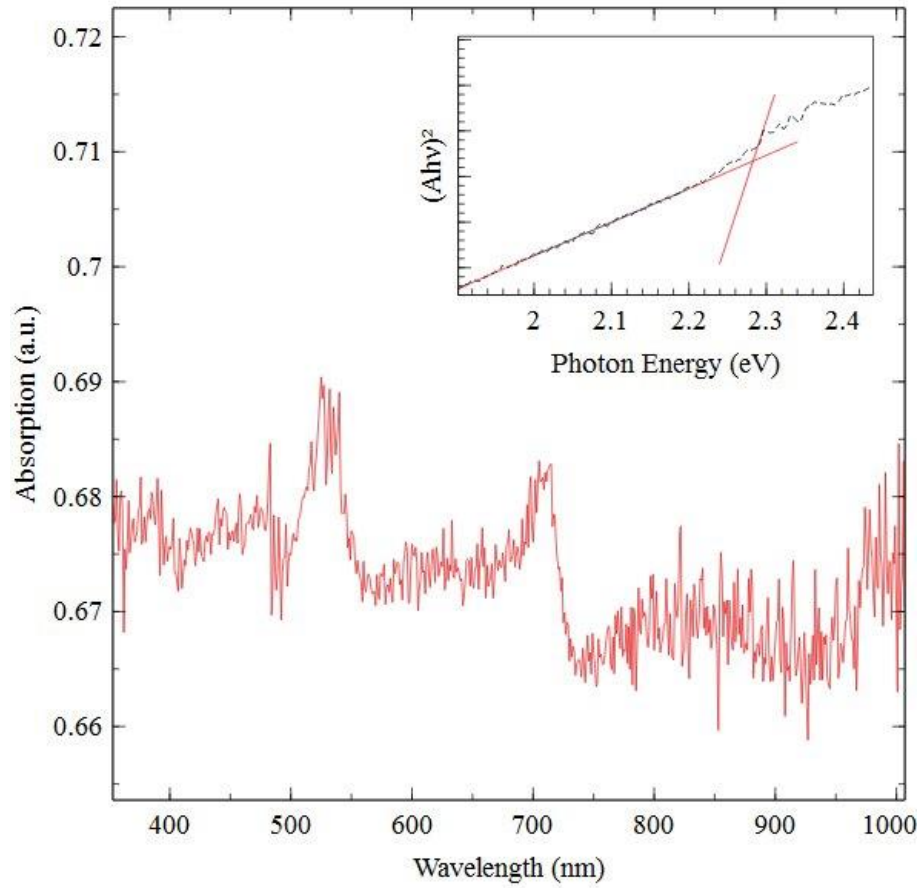


Figure 3. 7: UV-Vis spectrum for combination of CsI and BiI₃ in a 3:2 stoichiometric ratio with an estimated bandgap at 2.3 eV.

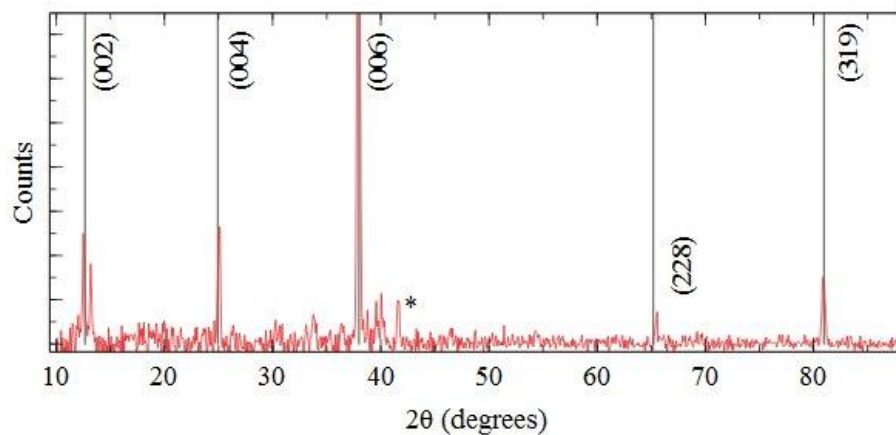


Figure 3. 8: XRD pattern of 3:2 ratio of CsI and BiI₃. Reference peaks of Cs₃Bi₂I₉ are tall vertical black lines. (*) indicates a BiI₃ reference peak. Peaks labeled with an asterisks (*) are attributed to CsI based on reference peaks in Appendix.

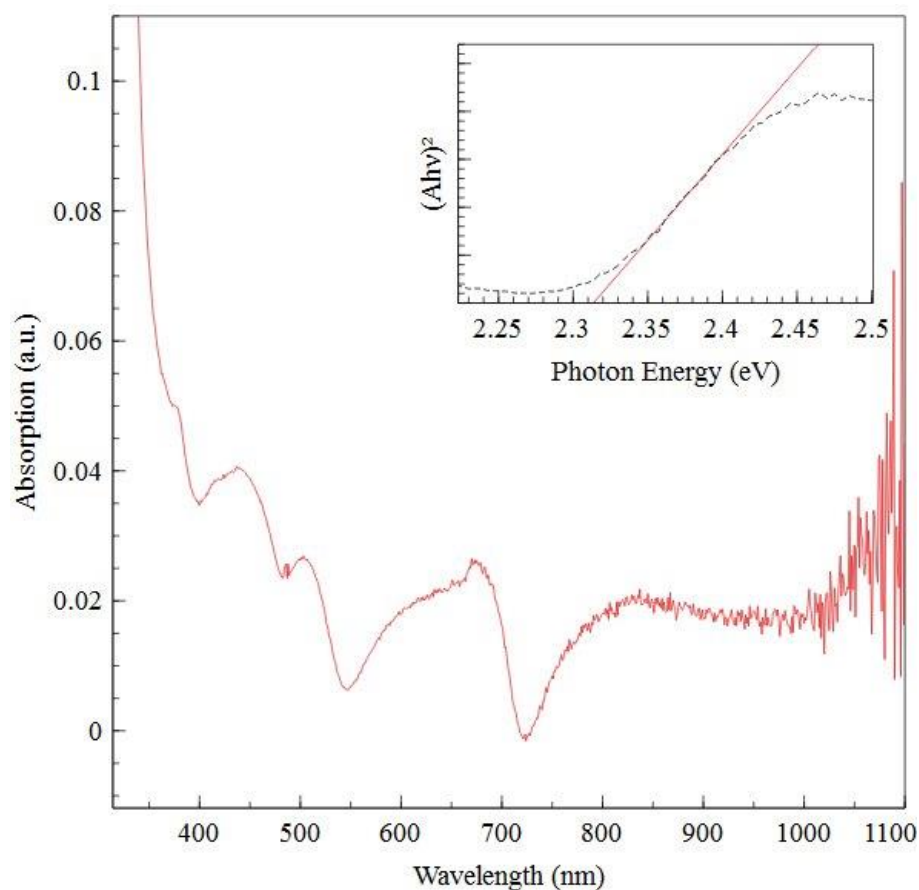


Figure 3. 9: UV-Vis spectrum and inset Tauc Plot for 3:2 ratio of FAI and BiI₃ with estimated bandgap at 2.31 eV.

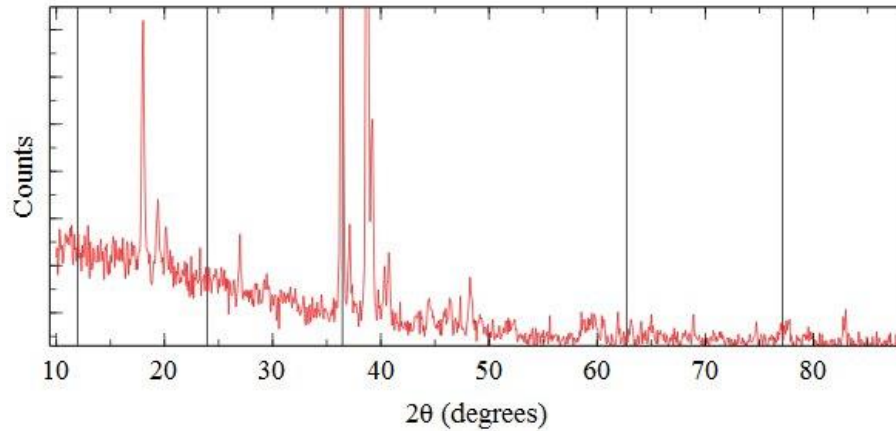


Figure 3. 10: XRD pattern of 3:2 ratio of FAI and BiI₃. Reference peaks of FA₃Bi₂I₉ are tall vertical black lines.

3.4.6 Antimony alloying of Low-Dimensional Bismuth Perovskite

3.4.6.1 Cs₃Bi_{2-x}Sb_xI₉

To probe the possibility of a tunable semiconductor, SbI₃ was combined with CsI and BiI₃. Since both Bi and Sb are trivalent cations with similar atomic radii, it is

conceivable that Sb could occupy the B-site and have an effect on the electrical properties of the film. The CsI, BiI₃, SbI₃ stoichiometric ratios are 3:1: x, where x= 0.3 or x=0.6.

UV-Vis spectra (**Figure 3.11** and **Figure 3.13**) show similar bandgap estimations around 2.3 eV for two levels of Sb alloying. Curiously, from the XRD patterns (compare **Figure 3.12** and **Figure 3.14**), an increase in Sb alloying shifted peaks to higher 2θ values. This suggests some substitution of Sb into the dioctahedrals, distorting the crystal structure slightly.

3.4.6.2 FA₃Bi_{2-x}Sb_xI₉

Similar to the previous section, SbI₃ was combined with FAI and BiI₃. Seen in **Figures 3.15 – 3.18**, UV-Vis spectra show similar bandgap estimations around 2.3 eV for two

levels of Sb alloying. XRD patterns show recrystallized precursor in the film. This is also seen in multiple bandgap transitions in the UV-Vis spectrum. There is no apparent shift in XRD peak positions. The UV-Vis spectrum does not show a significant change in estimated bandgaps in this series.

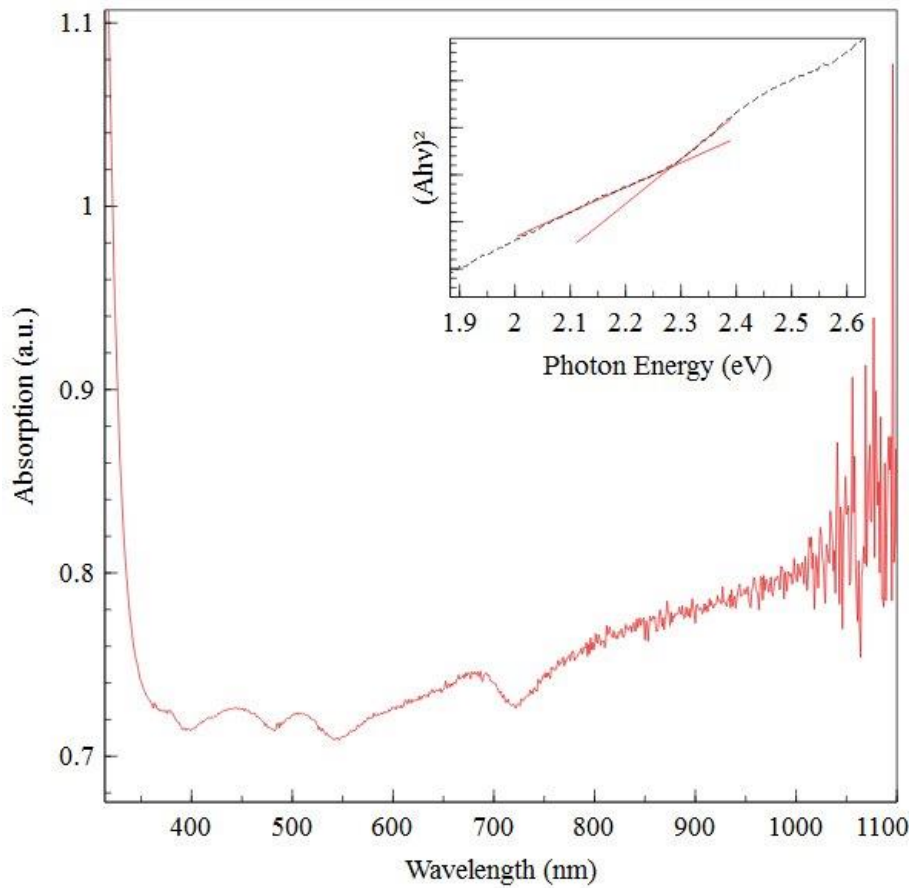


Figure 3. 11: UV-Vis spectrum for CsI, BiI₃, SbI₃ where x = 0.3

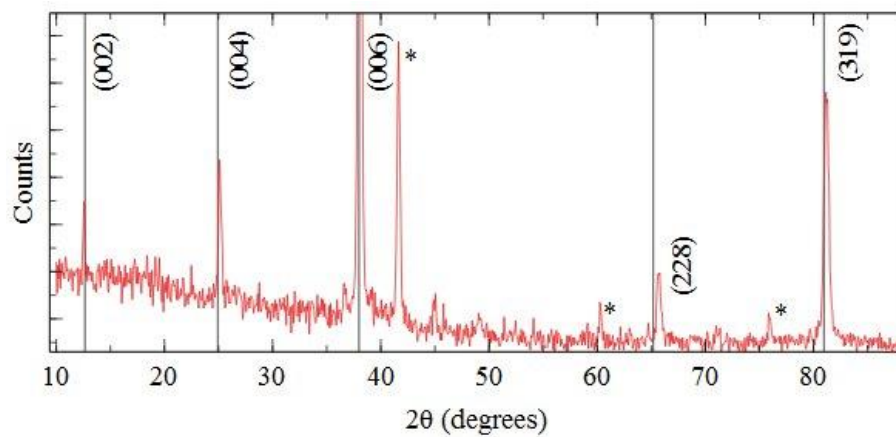


Figure 3. 12: XRD pattern for CsI, BiI₃, SbI₃ in a 3:1-x:x stoichiometric ratio where x = 0.3. Peaks labeled with an asterisks (*) are attributed to CsI based on reference peaks in Appendix. Vertical lines are reference peaks for Cs₃Bi₂I₉.

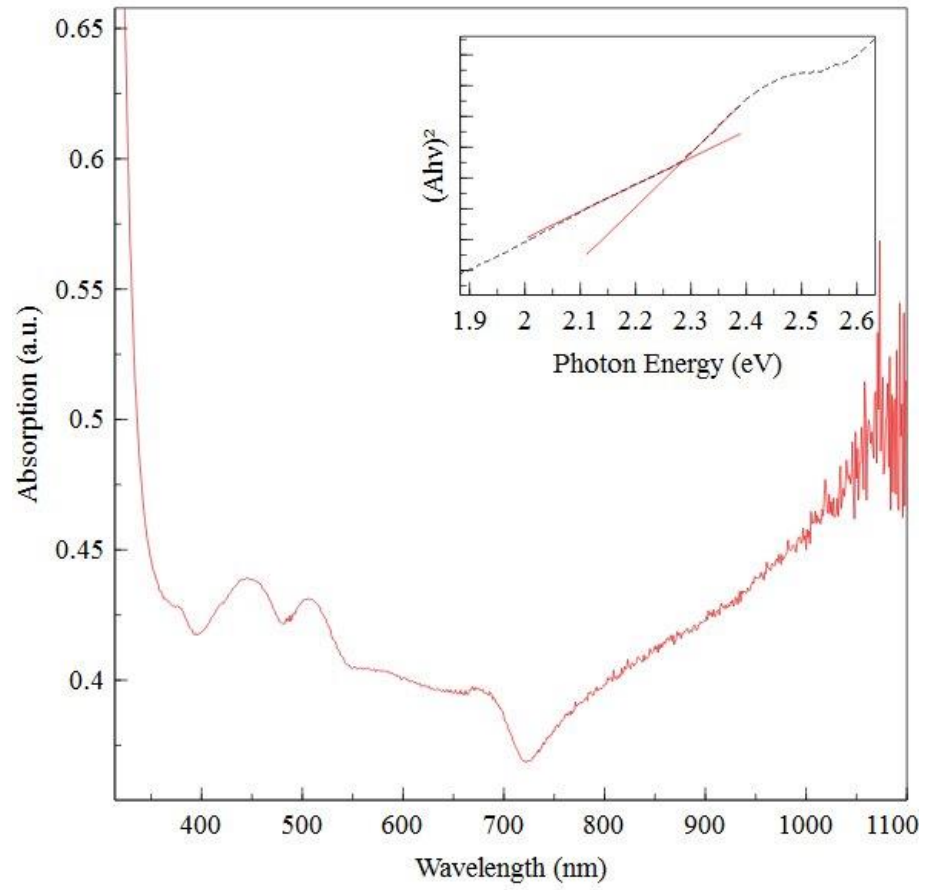


Figure 3. 13: UV-Vis spectrum for CsI, BiI₃, SbI₃ in a 3:1-x:x stoichiometric ratio where x = 0.6

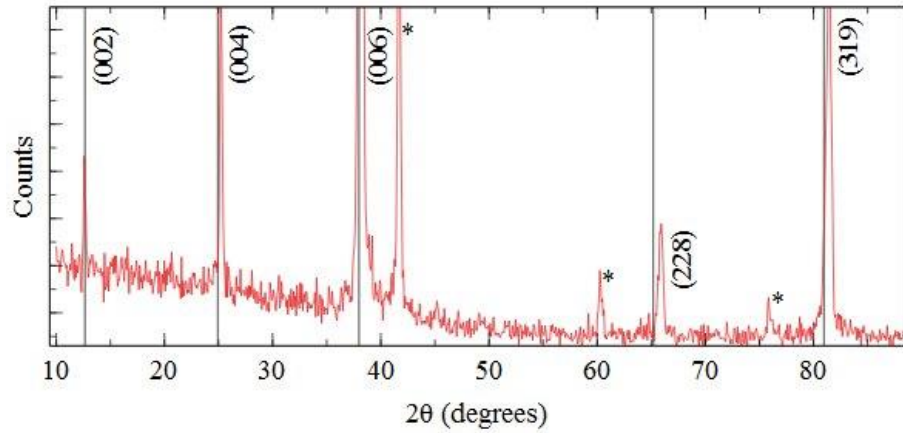


Figure 3. 14: XRD pattern for CsI, BiI₃, SbI₃ in a 3:1-x:x stoichiometric ratio where x = 0.6. Peaks labeled with an asterisks (*) are attributed to CsI based on reference peaks in Appendix. Vertical lines are reference peaks for Cs₃Bi₂I₉.

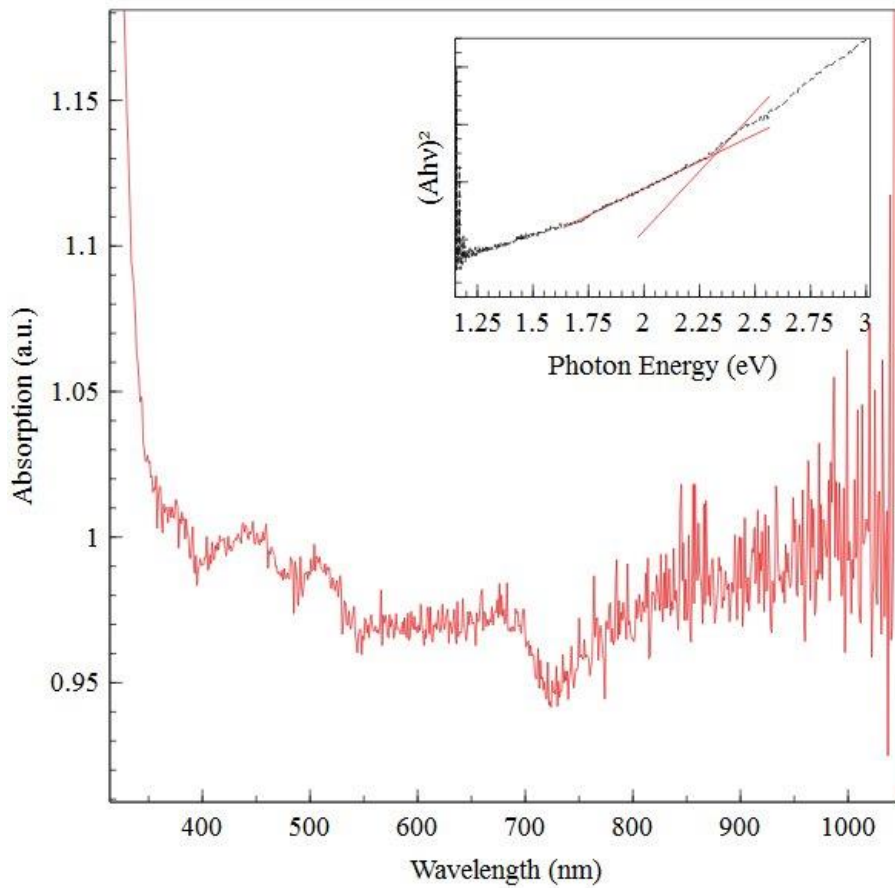


Figure 3. 15: UV-Vis spectrum for FAI, BiI₃, SbI₃ in a 3:1-x:x stoichiometric ratio where x = 0.3.

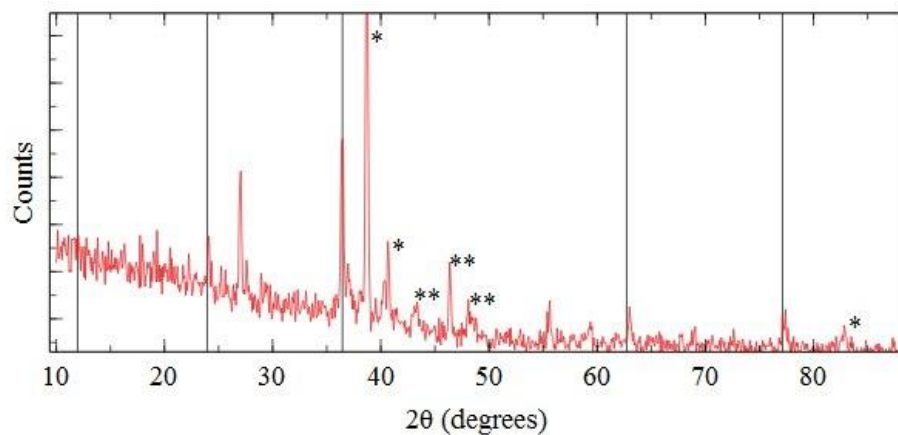


Figure 3. 16: XRD pattern for FAI, BiI₃, SbI₃ in a 3:1-x:x stoichiometric ratio where $x = 0.3$. Peaks labeled with an asterisks (*) are attributed to SbI₃ and (**) are attributed to FAI based on reference peaks in Appendix. Vertical lines are reference peaks for FA₃Bi₂I₉.

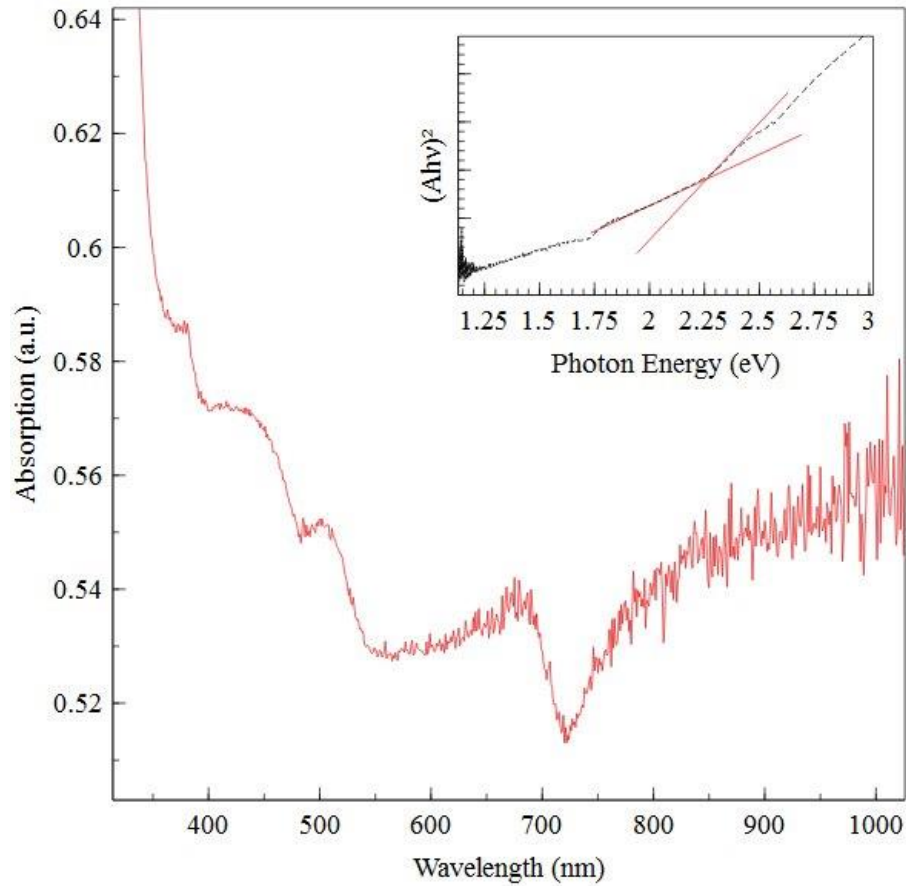


Figure 3. 17: UV-Vis spectrum for FAI, BiI₃, SbI₃ in a 3:1-x:x stoichiometric ratio where x = 0.6.

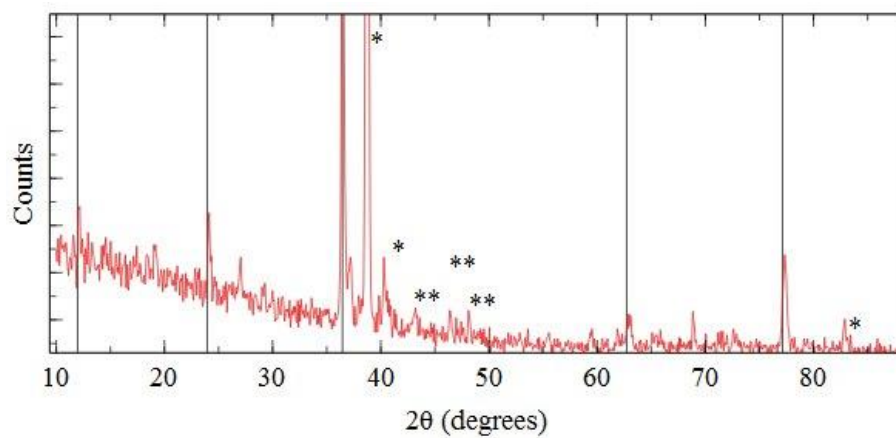


Figure 3. 18: XRD pattern for FAI, BiI₃, SbI₃ in a 3:1-x:x stoichiometric ratio where x = 0.6. Peaks labeled with an asterisks (*) are attributed to SbI₃ and (**) are attributed to FAI based on reference peaks in Appendix. Vertical lines are reference peaks for FA₃Bi₂I₉.

3.4.7 Low-Dimensional Antimony Perovskite

3.4.7.1 FA₃Sb₂I₉

An attempt was made to synthesis the antimony-based 0D perovskite using the same precursors used in previous experiments. The UV-Vis spectrum (**Figure 3.19**) shows a strong bandgap transition at 2.3 eV. The XRD pattern shows a pattern similar to the FA₃Bi₂I₉ pattern, indicating that the film has formed bioctahedral polymorphs. The XRD pattern (**Figure 3.20**) also shows some peaks from the SbI₃ precursors. It should be noted that SbI₃ is reported to have a bandgap of approximately 2.15 eV.⁷⁷ The observed bandgap could be affected by the presence of both compounds.

3.4.7.2 Cs₃Sb₂I₉

Using the CsI precursor, an attempt was made to synthesis zero-dimensional Cs₃Sb₂I₉. The UV-Vis (**Figure 3.21**) does not show an abrupt bandgap transition, so a bandgap estimation was not calculated. The XRD pattern (**Figure 3.22**) shows recrystallized precursors, with peaks corresponding to reference peaks of CsI and SbI₃. The XRD pattern does not show any peaks that are similar to the features seen in the previous zero-dimensional perovskites synthesized and characterized in this work. This particular sample experienced 6 days outside of the glovebox, which was longer than normal.

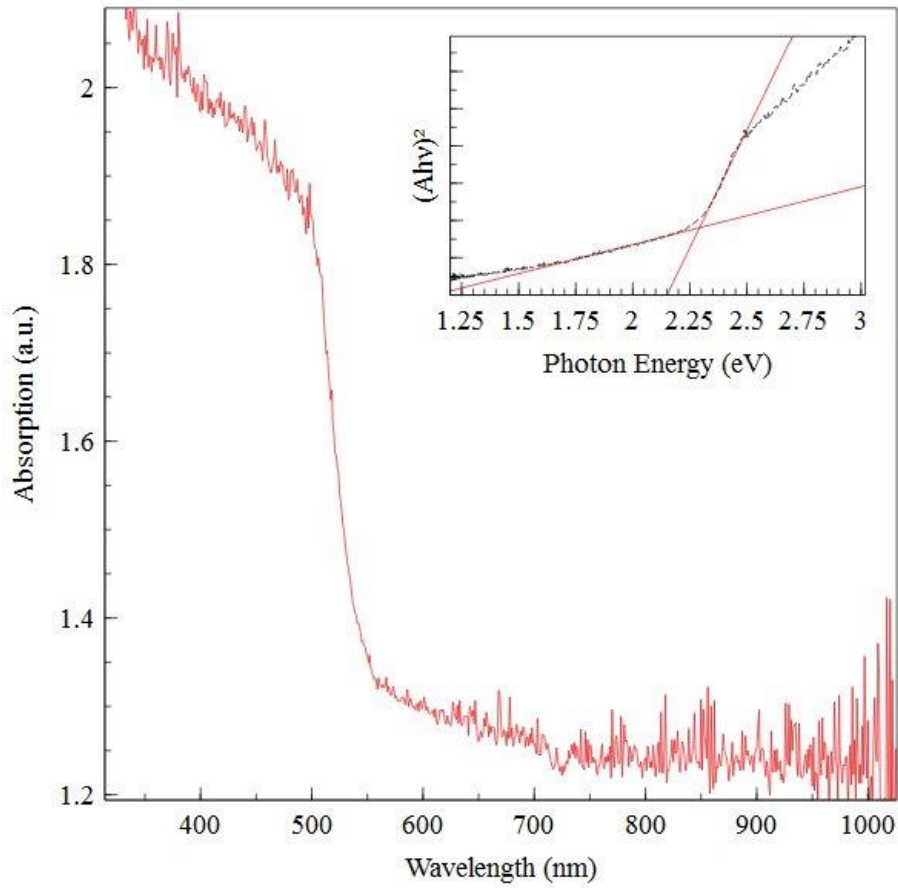


Figure 3. 19: UV-Vis spectrum of FAI and SbI_3 combined at a 3:2 ratio. Estimated bandgap is 2.3 eV.

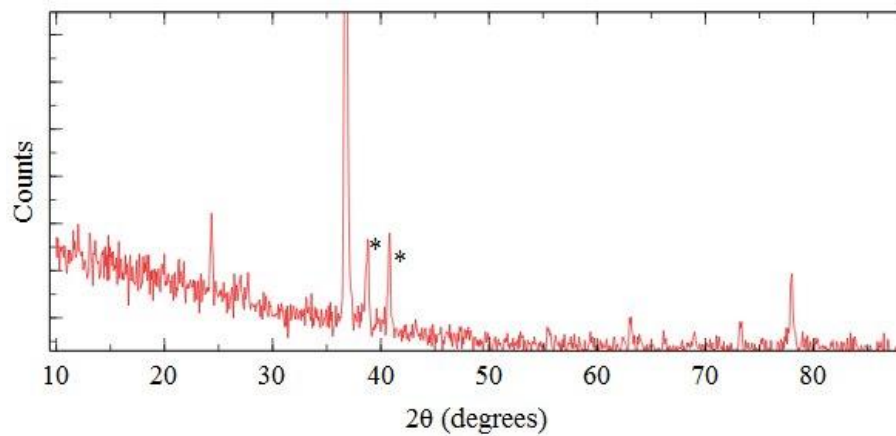


Figure 3. 20: XRD pattern from combination of FAI and SbI_3 in a 3:2 ratio. (*) indicates SbI_3 peaks.

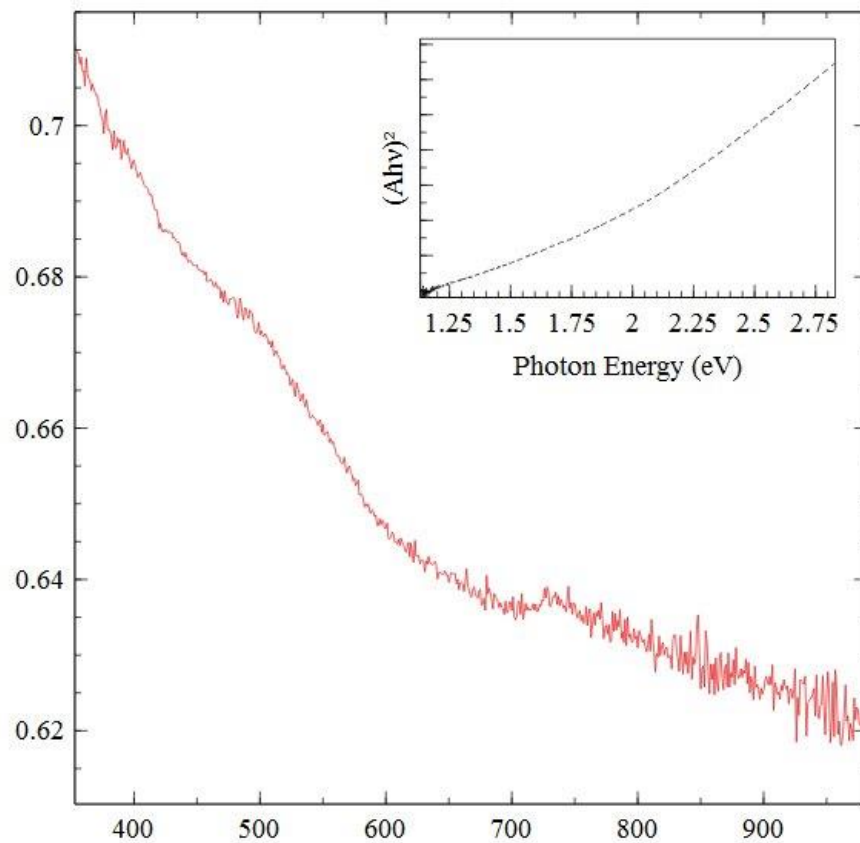


Figure 3. 21: UV-Vis spectrum of CsI and SbI_3 with no bandgap determination.

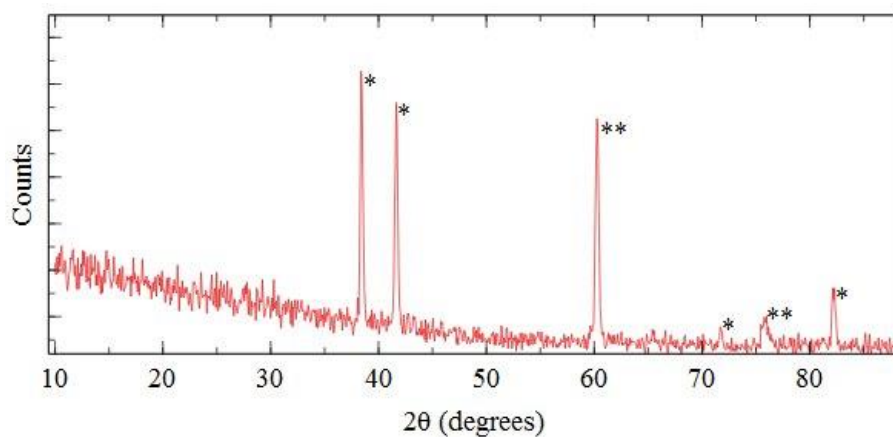


Figure 3. 22: XRD pattern of CsI and SbI_3 combined in a 3:2 ratio. (*) indicates SbI_3 peaks and (**) indicates CsI peaks.

4. Conclusion

Lead halide perovskite films have become the fastest growing solar technology in terms of efficiency. Discovering less toxic perovskite semiconductor materials will overcome a significant hurdle to widespread solar energy adoption. This work probed for perovskite structures of $A_2BB'X_6$ and $A_3B_2X_9$ where $A = \text{Cs}$ or FA , $B/B' = \text{Sn}, \text{Bi}, \text{Sb}, \text{and/or In}$ and $X = \text{I}$.

Theoretical calculations were referenced in order to guide experiment of low toxicity materials that exhibit similar electronic properties as the highly efficient lead halide perovskites. Theoretical calculations show double perovskites based on Bi & In or Sb & In using iodide as the halide potentially have narrow, direct bandgaps. However, experimentally these compounds were not formed by simple solution processing.

A lower-dimensional perovskite was uncovered while attempting to synthesize 3D double perovskite films. This compound is considered zero-dimensional since it is composed of two face-sharing octahedral creating a complex anion $(M_2X_9)^{3-}$ which is surrounded by three bulky cations, i.e. FA^+ or Cs^+ . XRD measurements show this compound is formed alongside recrystallized or residual precursor phases. Longer annealing times and moderate temperatures were shown to reduce the precursor phases for a particular series of experiments.

A series of films were made with slight tin-doping of the precursor solution, probing for a change in the electronic bandgap, as estimated by UV-Vis spectra and derived Tauc plots. A slight increase in estimated bandgaps was observed with an increase in tin-doping. This indicates there is a possibility to tune the electronic properties of the zero-dimensional $\text{FA}_3\text{Bi}_2\text{I}_9$ perovskite. The mechanism may be related to the addition of bystander atoms in the non-crystalline regions between each bioctahedral anion, either distorting the bonds or inducing an alternative alignment, which effectively tunes the electronic band structure.

Cs^+ was used in place of FA^+ as the A-site cation and $\text{Cs}_3\text{Bi}_2\text{I}_9$ perovskite was synthesized. Characterization by XRD indicated a similar zero-dimensional structure was made with the inorganic Cs^+ cation and matched reference XRD patterns. The bandgap value was similar to the FA^+ analog of this material, ~ 2.3 eV. BiI_3 precursor can be observed in the film by XRD reference peaks and by its narrow bandgap of ~ 1.7 eV observed in the UV-Vis spectrum.

Subsequent experiments focused on the zero-dimensional perovskite films of the form $\text{A}_3\text{B}_2\text{X}_9$, where $\text{A} = \text{Cs}^+$ or FA^+ , $\text{B} = \text{Bi}^{3+}$ and/or Sb^{3+} and $\text{X} = \text{I}^-$. $\text{Cs}_3\text{Bi}_{2-x}\text{Sb}_x\text{I}_9$ films were prepared and characterized by XRD, showing increase in 2θ angles in the diffraction pattern. This indicates an increased d-spacing in the structure of the low dimensional perovskite. UV-Vis does not show a significant change with respect to the estimated bandgap.

Low-dimensional perovskite films, where $\text{B} = \text{Sb}^{3+}$, were synthesized in the case where $\text{A} = \text{FA}^+$. UV-Vis indicated a strong bandgap transition at 2.3 eV. XRD patterns showed a

similar pattern to the bismuth analog, suggesting the zero-dimensional structure was formed.

This work has demonstrated the use of first principle calculations to inspire experimental investigations. Using elements suggested from theoretical calculations, possible combinations of metallic and organic iodide salts to create thin film semiconductors were explored. Characterization by XRD revealed a unique low-dimensional perovskite by simple solution processing. A systematic bandgap tuning of $\text{FA}_3\text{Bi}_2\text{I}_9$ by additive tin precursor alongside a spectator indium precursor was observed. Addition of SbI_3 precursor to film of $\text{Cs}_3\text{Bi}_2\text{I}_9$ showed a XRD peak shift, indicating a change in the spacing of the bioctahedral network that makes up the film. The UV-Vis spectrum did not uncover a shift in bandgap in this specific case. Tunable bandgaps have potential in higher efficiency tandem solar cells, where varying bandgaps can be stacked, resulting in more solar spectrum being harvested. Future work related to this research area may include use of different additives in an effort to tune the electronic properties or to induce the formation of lower direct bandgap films.

5. References

1. Neamen, Donald A. "Semiconductor Physics And Devices". New York, NY: McGraw-Hill, 2012.
2. Gadomski, Chris. "Global Investment Trends in Clean Energy". Dubai, UAE: Bloomberg New Energy Finance, 2016.
3. Stranks, Sam. "Revolutionizing solar power with perovskites". The Hello Tomorrow Global Summit, 2017.
4. Lunt, Richard. "See-Through Solar Harvesting Surfaces". Keynote: BMW Welcomes Smart Materials, 2015.
5. Riordan, M., and L. Hoddeson. "The Origins Of The Pn Junction". *IEEE Spectrum* 34, no. 6 (1997): 46-51. doi:10.1109/6.591664.
6. Smith, Willoughby. "Effect Of Light On Selenium During The Passage Of An Electric Current". *Nature* 7, no. 173 (1873): 303-303. doi:10.1038/007303e0.
7. Fritts, C. E. "On The Fritts Selenium Cells And Batteries". *Scientific American* 19, no. 492 (1885): 7854-7856. doi:10.1038/scientificamerican06061885-7854csupp.
8. Jean, Joel, Patrick R. Brown, Robert L. Jaffe, Tonio Buonassisi, and Vladimir Bulović. "Pathways For Solar Photovoltaics". *Energy & Environmental Science* 8, no. 4 (2015): 1200-1219. doi:10.1039/c4ee04073b.
9. Kingsbury, Edwin F., and Russell S. Ohl. "Photoelectric Properties Of Ionically Bombarded Silicon". *Bell System Technical Journal* 31, no. 4 (1952): 802-815. doi:10.1002/j.1538-7305.1952.tb01407.x.
10. Chapin, D. M., C. S. Fuller, and G. L. Pearson. "A New Silicon P-N Junction Photocell For Converting Solar Radiation Into Electrical Power". *Journal Of Applied Physics* 25, no. 5 (1954): 676-677. doi:10.1063/1.1721711.
11. Fraas, Lewis M. "Low-Cost Solar Electric Power", (2014). doi:10.1007/978-3-319-07530-3.
12. Lindmayer, J., and J.F. Allison. "The Violet Cell: An Improved Silicon Solar Cell". *Solar Cells* 29, no. 2-3 (1990): 151-166. doi:10.1016/0379-6787(90)90023-x.
13. Green, Martin A. "Forty Years Of Photovoltaic Research At UNSW". *Journal And Proceedings Of The Royal Society Of New South Wales* 148 (2015): 2-14.
14. Kumar, Abhishek, Monika Bieri, Thomas Reindl, and Armin G. Aberle. "Economic Viability Analysis Of Silicon Solar Cell Manufacturing: Al-BSF Versus PERC". *Energy Procedia* 130 (2017): 43-49. doi:10.1016/j.egypro.2017.09.412.
15. Anikeeva, Polina, Geoffrey Beach, and Niels Holten-Andersen. "MIT 3.024 Electronic, Optical And Magnetic Properties Of Materials". Lecture, Massachusetts Institute of Technology: MIT OpenCourseWare, <https://ocw.mit.edu/>. License: Creative Commons BY-NC-SA., 2013.

16. Archer, Mary D, and Martin A Green. *Clean Electricity From Photovoltaics*. 2nd ed. World Scientific, 2014.
17. Law, Daniel C., R.R. King, H. Yoon, M.J. Archer, A. Boca, C.M. Fetzer, S. Mesropian, T. Isshiki, M. Haddad, and K.M. Edmondson. "Future Technology Pathways Of Terrestrial III–V Multijunction Solar Cells For Concentrator Photovoltaic Systems". *Solar Energy Materials And Solar Cells* 94, no. 8 (2010): 1314-1318. doi:10.1016/j.solmat.2008.07.014.
18. Chopra, K. L., P. D. Paulson, and V. Dutta. "Thin-Film Solar Cells: An Overview". *Progress In Photovoltaics: Research And Applications* 12, no. 23 (2004): 69-92. doi:10.1002/pip.541.
19. Ludwigs, Sabine. "P3HT Revisited – From Molecular Scale to Solar Cells Devices". First Edition, 2014.
20. Smestad, G. and Gratzel, M. (1998). Demonstrating Electron Transfer and Nanotechnology: A Natural Dye-Sensitized Nanocrystalline Energy Converter. *Journal of Chemical Education*, 75(6), p.752.
21. Kojima, Akihiro, Kenjiro Teshima, Yasuo Shirai, and Tsutomu Miyasaka. "Organometal Halide Perovskites As Visible-Light Sensitizers For Photovoltaic Cells". *Journal Of The American Chemical Society* 131, no. 17 (2009): 6050-6051. doi:10.1021/ja809598r.
22. Kim, Hui-Seon, Chang-Ryul Lee, Jeong-Hyeok Im, Ki-Beom Lee, Thomas Moehl, Arianna Marchioro, and Soo-Jin Moon et al. "Lead Iodide Perovskite Sensitized All-Solid-State Submicron Thin Film Mesoscopic Solar Cell With Efficiency Exceeding 9%". *Scientific Reports* 2, no. 1 (2012). doi:10.1038/srep00591.
23. Lee, M. M., J. Teuscher, T. Miyasaka, T. N. Murakami, and H. J. Snaith. "Efficient Hybrid Solar Cells Based On Meso-Superstructured Organometal Halide Perovskites". *Science* 338, no. 6107 (2012): 643-647. doi:10.1126/science.1228604.
24. Liu, Mingzhen, Michael B. Johnston, and Henry J. Snaith. "Efficient Planar Heterojunction Perovskite Solar Cells By Vapour Deposition". *Nature* 501, no. 7467 (2013): 395-398. doi:10.1038/nature12509.
25. Park, Nam-Gyu, Michael Grätzel, and Tsutomu Miyasaka. *Organic-Inorganic Halide Perovskite Photovoltaics*. Cham: Springer International Publishing, 2016.
26. "Contributed Papers In Specimen Mineralogy: 38Th Rochester Mineralogical Symposium Abstracts: Part 3". *Rocks & Minerals* 87, no. 5 (2012): 444-454. doi:10.1080/00357529.2012.716338.
27. Weber, Dieter. "CH₃NH₃PbX₃, A Pb(II)-System With Cubic Perovskite Structure". *Zeitschrift Für Naturforschung B* 33, no. 12 (1978): 1443-1445. doi:10.1515/znb-1978-1214.
28. Mitzi, D. B., S. Wang, C. A. Feild, C. A. Chess, and A. M. Guloy. "Conducting Layered Organic-Inorganic Halides Containing <110>-Oriented Perovskite Sheets". *Science* 267, no. 5203 (1995): 1473-1476. doi:10.1126/science.267.5203.1473.

29. Brittman, Sarah, Gede Widia Pratama Adhyaksa, and Erik Christian Garnett. "The Expanding World Of Hybrid Perovskites: Materials Properties And Emerging Applications". *MRS Communications* 5, no. 01 (2015): 7-26. doi:10.1557/mrc.2015.6.
30. Diao Wei-Guang, Eric, and Peter Chen Chao-Yu. *Perovskite Solar Cells*. 1st ed. Singapore: World Scientific, 2018.
31. Cui, Jin, Huailiang Yuan, Junpeng Li, Xiaobao Xu, Yan Shen, Hong Lin, and Mingkui Wang. "Recent Progress In Efficient Hybrid Lead Halide Perovskite Solar Cells". *Science And Technology Of Advanced Materials* 16, no. 3 (2015): 036004. doi:10.1088/1468-6996/16/3/036004.
32. Schueller, Emily C., Geneva Laurita, Douglas H. Fabini, Constantinos C. Stoumpos, Mercouri G. Kanatzidis, and Ram Seshadri. "Crystal Structure Evolution And Notable Thermal Expansion In Hybrid Perovskites Formamidinium Tin Iodide And Formamidinium Lead Bromide". *Inorganic Chemistry* 57, no. 2 (2017): 695-701. doi:10.1021/acs.inorgchem.7b02576.
33. Oku, Takeo. "Crystal Structures Of CH₃NH₃PbI₃ And Related Perovskite Compounds Used For Solar Cells". *Solar Cells - New Approaches And Reviews*, 2015. doi:10.5772/59284.
34. Zhang, Hua, Xianfeng Qiao, Yan Shen, Thomas Moehl, Shaik M. Zakeeruddin, Michael Grätzel, and Mingkui Wang. "Photovoltaic Behaviour Of Lead Methylammonium Triiodide Perovskite Solar Cells Down To 80 K". *Journal Of Materials Chemistry A* 3, no. 22 (2015): 11762-11767. doi:10.1039/c5ta02206a.
35. Baikie, Tom, Nathan S. Barrow, Yanan Fang, Philip J. Keenan, Peter R. Slater, Ross O. Piltz, Matthias Gutmann, Subodh G. Mhaisalkar, and Tim J. White. "A Combined Single Crystal Neutron/X-Ray Diffraction And Solid-State Nuclear Magnetic Resonance Study Of The Hybrid Perovskites CH₃NH₃PbX₃ (X = I, Br And Cl)". *Journal Of Materials Chemistry A* 3, no. 17 (2015): 9298-9307. doi:10.1039/c5ta01125f.
36. Bouclé, Johann, and Nathalie Herlin-Boime. "The Benefits Of Graphene For Hybrid Perovskite Solar Cells". *Synthetic Metals* 222 (2016): 3-16. doi:10.1016/j.synthmet.2016.03.030.
37. Eperon, Giles E., Samuel D. Stranks, Christopher Menelaou, Michael B. Johnston, Laura M. Herz, and Henry J. Snaith. "Formamidinium Lead Trihalide: A Broadly Tunable Perovskite For Efficient Planar Heterojunction Solar Cells". *Energy & Environmental Science* 7, no. 3 (2014): 982. doi:10.1039/c3ee43822h.
38. Eperon, Giles E., Tomas Leijtens, Kevin A. Bush, Rohit Prasanna, Thomas Green, Jacob Tse-Wei Wang, and David P. McMeekin et al. "Perovskite-Perovskite Tandem Photovoltaics With Optimized Band Gaps". *Science* 354, no. 6314 (2016): 861-865. doi:10.1126/science.aaf9717.
39. Ahn, Namyong, Seong Min Kang, Jin-Wook Lee, Mansoo Choi, and Nam-Gyu Park. "Thermodynamic Regulation Of CH₃NH₃PbI₃ Crystal Growth And Its Effect On Photovoltaic Performance Of Perovskite Solar Cells". *Journal Of Materials Chemistry A* 3, no. 39 (2015): 19901-19906. doi:10.1039/c5ta03990h.

40. Kim, Dong Hoe, Jaehong Park, Zhen Li, Mengjin Yang, Ji-Sang Park, Ik Jae Park, Jin Young Kim, Joseph J. Berry, Garry Rumbles, and Kai Zhu. "300% Enhancement Of Carrier Mobility In Uniaxial-Oriented Perovskite Films Formed By Topotactic-Oriented Attachment". *Advanced Materials* 29, no. 23 (2017): 1606831. doi:10.1002/adma.201606831.
41. Li, Shuigen, Chen Zhang, Jiao-Jiao Song, Xiaohu Xie, Jian-Qiao Meng, and Shunjian Xu. "Metal Halide Perovskite Single Crystals: From Growth Process To Application". *Crystals* 8, no. 5 (2018): 220. doi:10.3390/cryst8050220.
42. Song, Tze-Bin, Qi Chen, Huanping Zhou, Chengyang Jiang, Hsin-Hua Wang, Yang (Michael) Yang, Yongsheng Liu, Jingbi You, and Yang Yang. "Perovskite Solar Cells: Film Formation And Properties". *Journal Of Materials Chemistry A* 3, no. 17 (2015): 9032-9050. doi:10.1039/c4ta05246c.
43. Saliba, Michael, Juan-Pablo Correa-Baena, Christian M. Wolff, Martin Stollerfoht, Nga Phung, Steve Albrecht, Dieter Neher, and Antonio Abate. "How To Make Over 20% Efficient Perovskite Solar Cells In Regular (N-I-P) And Inverted (P-I-N) Architectures". *Chemistry Of Materials* 30, no. 13 (2018): 4193-4201. doi:10.1021/acs.chemmater.8b00136.
44. You, Hongjun, and Jixiang Fang. "Particle-Mediated Nucleation And Growth Of Solution-Synthesized Metal Nanocrystals: A New Story Beyond The Lamer Curve". *Nano Today* 11, no. 2 (2016): 145-167. doi:10.1016/j.nantod.2016.04.003.
45. Yan, Keyou, Mingzhu Long, Tiankai Zhang, Zhanhua Wei, Haining Chen, Shihe Yang, and Jianbin Xu. "Hybrid Halide Perovskite Solar Cell Precursors: Colloidal Chemistry And Coordination Engineering Behind Device Processing For High Efficiency". *Journal Of The American Chemical Society* 137, no. 13 (2015): 4460-4468. doi:10.1021/jacs.5b00321.
46. Moore, David T., Hiroaki Sai, Kwan W. Tan, Detlef-M. Smilgies, Wei Zhang, Henry J. Snaith, Ulrich Wiesner, and Lara A. Estroff. "Crystallization Kinetics Of Organic-Inorganic Trihalide Perovskites And The Role Of The Lead Anion In Crystal Growth". *Journal Of The American Chemical Society* 137, no. 6 (2015): 2350-2358. doi:10.1021/ja512117e.
47. Pang, Yuepeng, Dongke Sun, Qinfen Gu, Kuo-Chih Chou, Xunli Wang, and Qian Li. "Comprehensive Determination Of Kinetic Parameters In Solid-State Phase Transitions: An Extended Jonhson-Mehl-Avrami-Kolomogorov Model With Analytical Solutions". *Crystal Growth & Design* 16, no. 4 (2016): 2404-2415. doi:10.1021/acs.cgd.6b00187.
48. Lee, Jin-Wook, Hui-Seon Kim, and Nam-Gyu Park. "Lewis Acid-Base Adduct Approach For High Efficiency Perovskite Solar Cells". *Accounts Of Chemical Research* 49, no. 2 (2016): 311-319. doi:10.1021/acs.accounts.5b00440.
49. Liu, Dianyi, and Timothy L. Kelly. "Perovskite Solar Cells With A Planar Heterojunction Structure Prepared Using Room-Temperature Solution Processing Techniques". *Nature Photonics* 8, no. 2 (2013): 133-138. doi:10.1038/nphoton.2013.342.

50. Tidhar, Yaron, Eran Edri, Haim Weissman, Dorin Zohar, Gary Hodes, David Cahen, Boris Rybtchinski, and Saar Kirmayer. "Crystallization Of Methyl Ammonium Lead Halide Perovskites: Implications For Photovoltaic Applications". *Journal Of The American Chemical Society* 136, no. 38 (2014): 13249-13256. doi:10.1021/ja505556s.
51. Slavney, Adam H., Te Hu, Aaron M. Lindenberg, and Hemamala I. Karunadasa. "A Bismuth-Halide Double Perovskite With Long Carrier Recombination Lifetime For Photovoltaic Applications". *Journal Of The American Chemical Society* 138, no. 7 (2016): 2138-2141. doi:10.1021/jacs.5b13294.
52. Yang, Bin, Ya-Juan Li, Yu-Xuan Tang, Xin Mao, Cheng Luo, Mei-Shan Wang, Wei-Qiao Deng, and Ke-Li Han. "Constructing Sensitive And Fast Lead-Free Single-Crystalline Perovskite Photodetectors". *The Journal Of Physical Chemistry Letters* 9, no. 11 (2018): 3087-3092. doi:10.1021/acs.jpcllett.8b01116.
53. Saidaminov, Makhsud I., Ahmed L. Abdelhady, Giacomo Maculan, and Osman M. Bakr. "Retrograde Solubility Of Formamidinium And Methylammonium Lead Halide Perovskites Enabling Rapid Single Crystal Growth". *Chemical Communications* 51, no. 100 (2015): 17658-17661. doi:10.1039/c5cc06916e.
54. Prochowicz, D., M. Franckevičius, A. M. Cieślak, S. M. Zakeeruddin, M. Grätzel, and J. Lewiński. "Mechanosynthesis Of The Hybrid Perovskite $\text{CH}_3\text{NH}_3\text{PbI}_3$: Characterization And The Corresponding Solar Cell Efficiency". *Journal Of Materials Chemistry A* 3, no. 41 (2015): 20772-20777. doi:10.1039/c5ta04904k.
55. Yang, Jinli, Braden D. Siempelkamp, Dianyi Liu, and Timothy L. Kelly. "Investigation Of $\text{CH}_3\text{NH}_3\text{PbI}_3$ Degradation Rates And Mechanisms In Controlled Humidity Environments Using In Situ Techniques". *ACS Nano* 9, no. 2 (2015): 1955-1963. doi:10.1021/nn506864k.
56. Stranks, S. D., G. E. Eperon, G. Grancini, C. Menelaou, M. J. P. Alcocer, T. Leijtens, L. M. Herz, A. Petrozza, and H. J. Snaith. "Electron-Hole Diffusion Lengths Exceeding 1 Micrometer In An Organometal Trihalide Perovskite Absorber". *Science* 342, no. 6156 (2013): 341-344. doi:10.1126/science.1243982.
57. Cumberbatch, T.J., and D.C. Northrop. "Bias-Dependent Radiation Damage In Diffused Silicon Solar Cells". *Solar Cells* 2, no. 1 (1980): 77-84. doi:10.1016/0379-6787(80)90101-5.
58. Chen, Bo, Mengjin Yang, Shashank Priya, and Kai Zhu. "Origin Of J-V Hysteresis In Perovskite Solar Cells". *The Journal Of Physical Chemistry Letters* 7, no. 5 (2016): 905-917. doi:10.1021/acs.jpcllett.6b00215.
59. Tress, Wolfgang, Nevena Marinova, Olle Inganäs, Mohammad. K. Nazeeruddin, Shaik M. Zakeeruddin, and Michael Graetzel. "Predicting The Open-Circuit Voltage Of $\text{CH}_3\text{NH}_3\text{PbI}_3$ perovskite Solar Cells Using Electroluminescence And Photovoltaic Quantum Efficiency Spectra: The Role Of Radiative And Non-Radiative Recombination". *Advanced Energy Materials* 5, no. 3 (2014): 1400812. doi:10.1002/aenm.201400812.
60. Noel, Nakita K., Samuel D. Stranks, Antonio Abate, Christian Wehrenfennig, Simone Guarnera, Amir-Abbas Haghighirad, and Aditya Sadhanala et al. "Lead-Free Organic-Inorganic Tin Halide Perovskites For Photovoltaic Applications". *Energy Environ. Sci.* 7, no. 9 (2014): 3061-3068. doi:10.1039/c4ee01076k.

61. Liao, Yuqin, Hefei Liu, Wenjia Zhou, Dongwen Yang, Yuequn Shang, Zhifang Shi, and Binghan Li et al. "Highly Oriented Low-Dimensional Tin Halide Perovskites With Enhanced Stability And Photovoltaic Performance". *Journal Of The American Chemical Society* 139, no. 19 (2017): 6693-6699. doi:10.1021/jacs.7b01815.
62. Liao, Weiqiang, Dewei Zhao, Yue Yu, Corey R. Grice, Changlei Wang, Alexander J. Cimaroli, and Philip Schulz et al. "Lead-Free Inverted Planar Formamidinium Tin Triiodide Perovskite Solar Cells Achieving Power Conversion Efficiencies Up To 6.22%". *Advanced Materials* 28, no. 42 (2016): 9333-9340. doi:10.1002/adma.201602992.
63. Arakcheeva, A. V., M. Bonin, G. Chapis, and A. I. Zaitsev. "The Phases Of Cs₃Bi₂I₉ Between RT And 190 K". *Zeitschrift Für Kristallographie - Crystalline Materials* 214, no. 5 (1999). doi:10.1524/zkri.1999.214.5.279.
64. Eckhardt, Kai, Volodymyr Bon, Jürgen Getzschmann, Julia Grothe, Florian M. Wieser, and Stefan Kaskel. "Crystallographic Insights Into (CH₃NH₃)₃(Bi₂I₉): A New Lead-Free Hybrid Organic–Inorganic Material As A Potential Absorber For Photovoltaics". *Chemical Communications* 52, no. 14 (2016): 3058-3060. doi:10.1039/c5cc10455f.
65. Hong, Ki-Ha, Jongseob Kim, Lamjed Debbichi, Hyungjun Kim, and Sang Hyuk Im. "Band Gap Engineering Of Cs₃Bi₂I₉ Perovskites With Trivalent Atoms Using A Dual Metal Cation". *The Journal Of Physical Chemistry C* 121, no. 1 (2016): 969-974. doi:10.1021/acs.jpcc.6b12426.
66. Ghosh, Biplab, Sudip Chakraborty, Hao Wei, Claude Guet, Shuzhou Li, Subodh Mhaisalkar, and Nripan Mathews. "Poor Photovoltaic Performance Of Cs₃Bi₂I₉: An Insight Through First-Principles Calculations". *The Journal Of Physical Chemistry C* 121, no. 32 (2017): 17062-17067. doi:10.1021/acs.jpcc.7b03501.
67. Xiao, Zewen, Ke-Zhao Du, Weiwei Meng, Jianbo Wang, David B. Mitzi, and Yanfa Yan. "Correction To "Intrinsic Instability Of Cs₂In(I)M(III)X₆ (M = Bi, Sb; X = Halogen) Double Perovskites: A Combined Density Functional Theory And Experimental Study"". *Journal Of The American Chemical Society* 139, no. 27 (2017): 9409-9409. doi:10.1021/jacs.7b06199.
68. Wei, Fengxia, Zeyu Deng, Shijing Sun, Fenghua Zhang, Donald M. Evans, Gregor Kieslich, and Satoshi Tominaka et al. "Synthesis And Properties Of A Lead-Free Hybrid Double Perovskite: (CH₃NH₃)₂AgBiBr₆". *Chemistry Of Materials* 29, no. 3 (2017): 1089-1094. doi:10.1021/acs.chemmater.6b03944.
69. Volonakis, George, Amir Abbas Haghighirad, Henry J. Snaith, and Feliciano Giustino. "Route To Stable Lead-Free Double Perovskites With The Electronic Structure Of CH₃NH₃PbI₃: A Case For Mixed-Cation [Cs/CH₃NH₃/CH(NH₂)₂]₂InBiBr₆". *The Journal Of Physical Chemistry Letters* 8, no. 16 (2017): 3917-3924. doi:10.1021/acs.jpcllett.7b01584.
70. Volonakis, George, Amir Abbas Haghighirad, Rebecca L. Milot, Weng H. Sio, Marina R. Filip, Bernard Wenger, Michael B. Johnston, Laura M. Herz, Henry J. Snaith, and Feliciano Giustino. "Cs₂InAgCl₆: A New Lead-Free Halide Double Perovskite With Direct Band Gap". *The Journal Of Physical Chemistry Letters* 8, no. 4 (2017): 772-778. doi:10.1021/acs.jpcllett.6b02682.

71. Nakajima, Takahito, and Keisuke Sawada. "Discovery Of Pb-Free Perovskite Solar Cells Via High-Throughput Simulation On The K Computer". *The Journal Of Physical Chemistry Letters* 8, no. 19 (2017): 4826-4831. doi:10.1021/acs.jpcelett.7b02203.
72. Huang, Xing, Su Huang, Pratim Biswas, and Rohan Mishra. "Band Gap Insensitivity To Large Chemical Pressures In Ternary Bismuth Iodides For Photovoltaic Applications". *The Journal Of Physical Chemistry C* 120, no. 51 (2016): 28924-28932. doi:10.1021/acs.jpcc.6b09567.
73. Lehner, Anna J., Douglas H. Fabini, Hayden A. Evans, Claire-Alice Hébert, Sara R. Smock, Jerry Hu, Hengbin Wang, Josef W. Zwanziger, Michael L. Chabiny, and Ram Seshadri. "Crystal And Electronic Structures Of Complex Bismuth Iodides $A_3Bi_2I_9$ ($A = K, Rb, Cs$) Related To Perovskite: Aiding The Rational Design Of Photovoltaics". *Chemistry Of Materials* 27, no. 20 (2015): 7137-7148. doi:10.1021/acs.chemmater.5b03147.
74. Tauc, J., R. Grigorovici, and A. Vancu. "Optical Properties And Electronic Structure Of Amorphous Germanium". *Physica Status Solidi (B)* 15, no. 2 (1966): 627-637. doi:10.1002/pssb.19660150224.
75. Triloki, P. Garg, R. Rai, and B.K. Singh. "Structural Characterization Of "As-Deposited" Cesium Iodide Films Studied By X-Ray Diffraction And Transmission Electron Microscopy Techniques". *Nuclear Instruments And Methods In Physics Research Section A: Accelerators, Spectrometers, Detectors And Associated Equipment* 736 (2014): 128-134. doi:10.1016/j.nima.2013.10.075.
76. Mosconi, Edoardo, Paolo Umari, and Filippo De Angelis. "Electronic And Optical Properties Of Mixed Sn–Pb Organohalide Perovskites: A First Principles Investigation". *Journal Of Materials Chemistry A* 3, no. 17 (2015): 9208-9215. doi:10.1039/c4ta06230b.
77. Lindqvist, Oliver, Georg Johansson, Finn Sandberg, and Torbjörn Norin. "The Crystal Structure Of Cesium Bismuth Iodide, $Cs_3Bi_2I_9$ ". *Acta Chemica Scandinavica* 22 (1968): 2943-2952. doi:10.3891/acta.chem.scand.22-2943.

6. Appendix

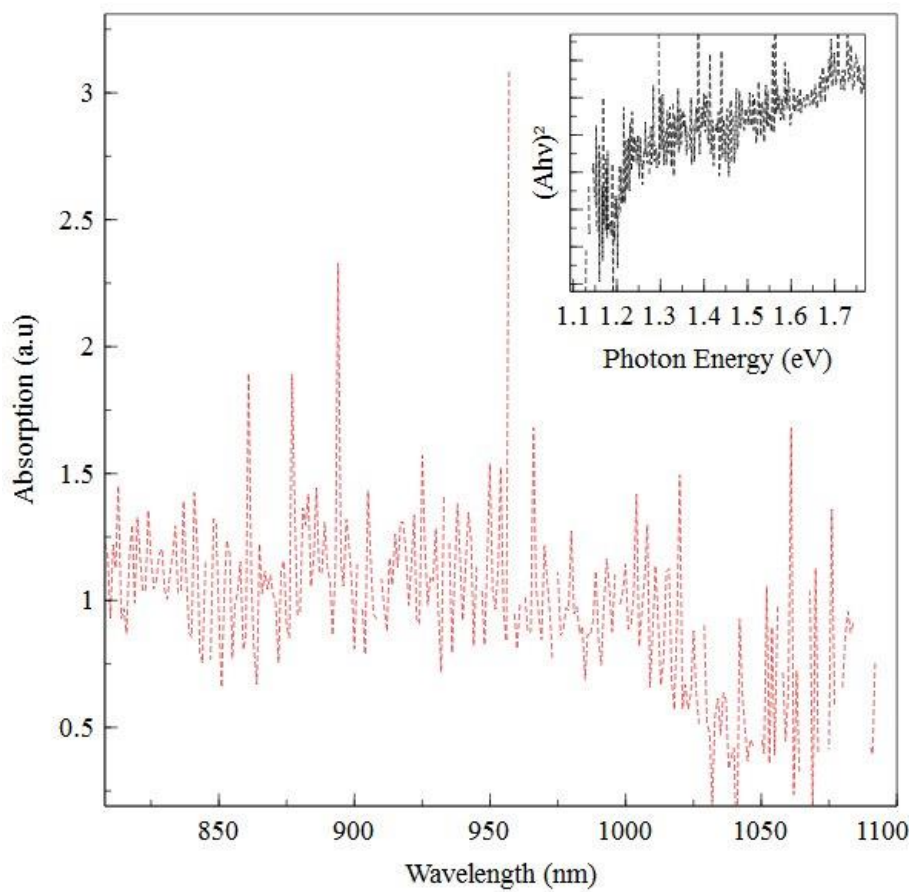


Figure 6. 1: UV-Vis spectrum of combination of FAI, SbI₃ and InI.

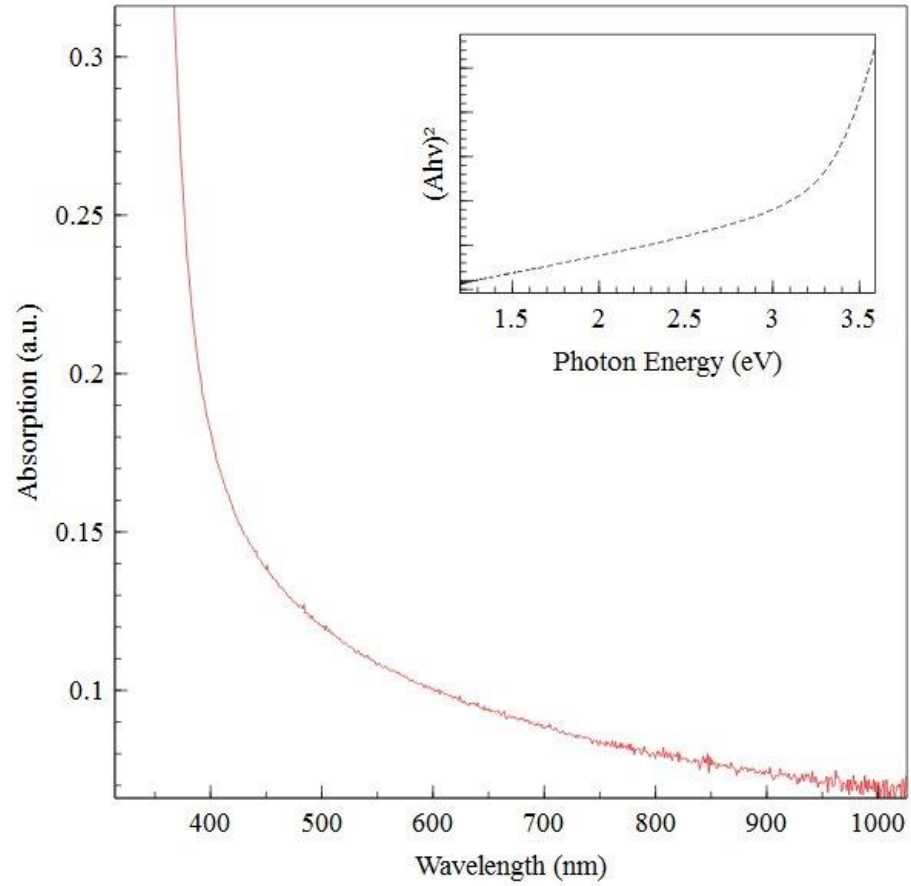
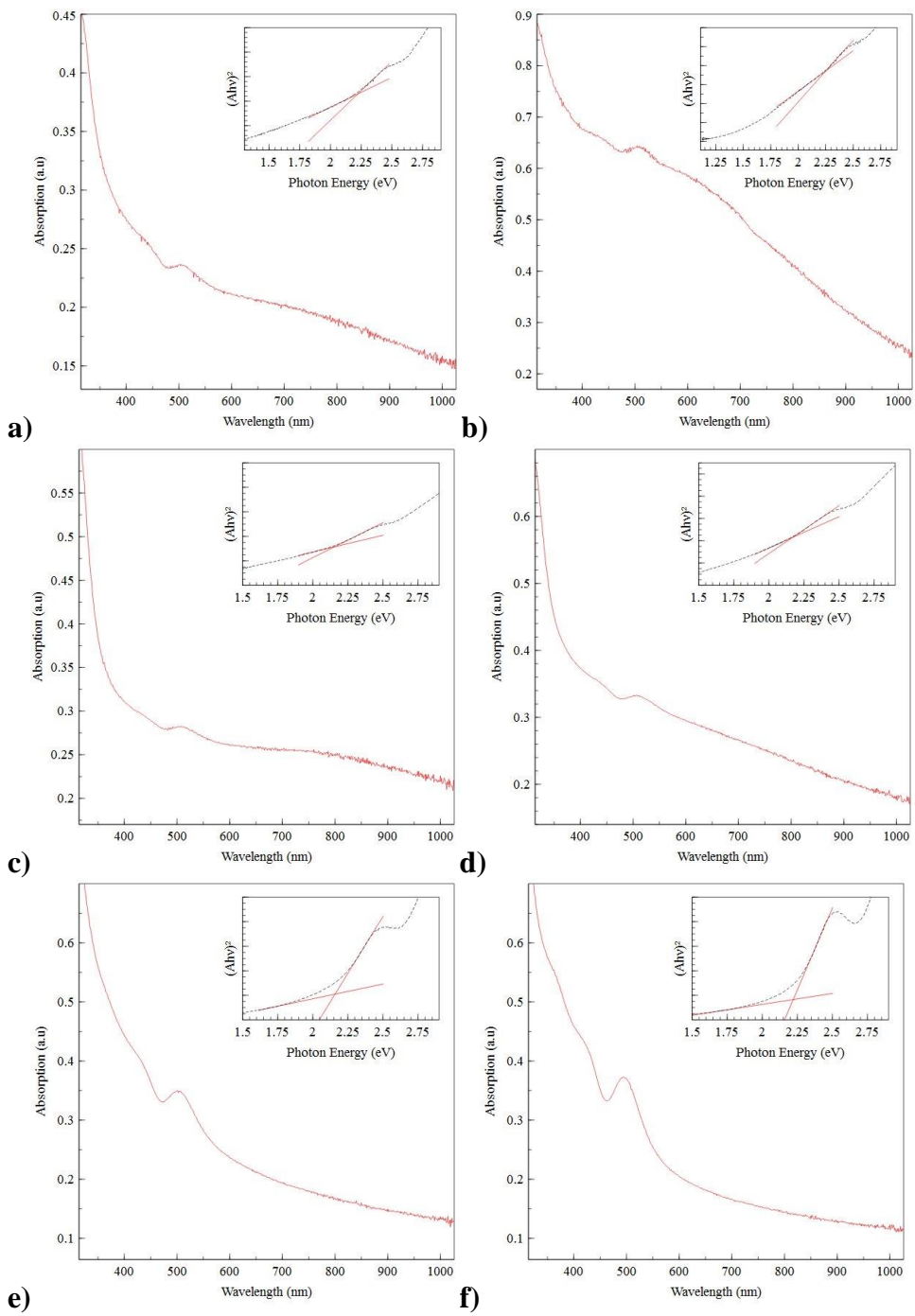


Figure 6. 2: UV Vis spectrum of FAI, SbI₃ and InI combined in a 3:1:1 stoichiometric ratio.



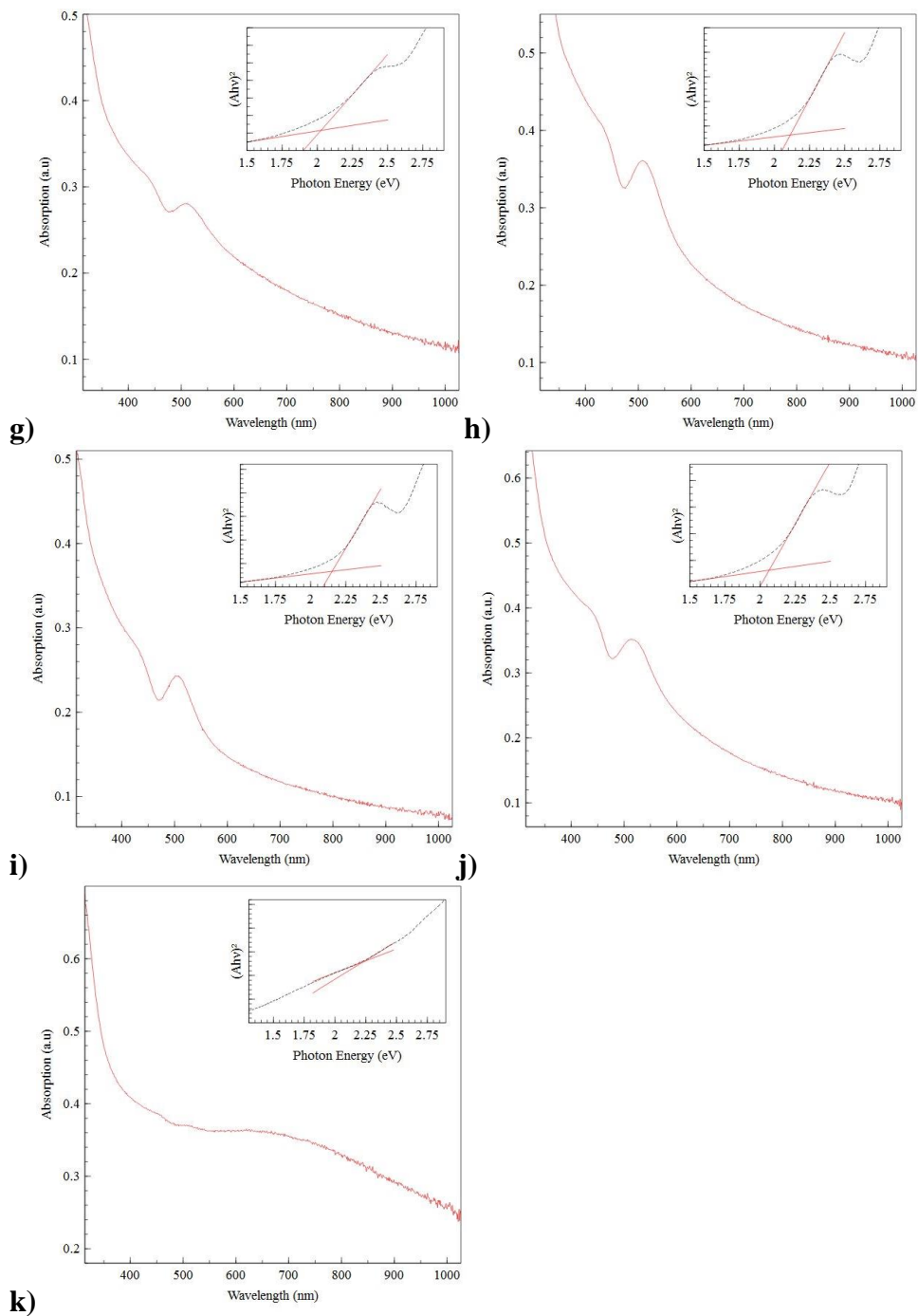


Figure 6. 3: UV-Vis spectra resulting from combination of FAI, BiI₃, InI and doping of x mol % SnI₂/0.2SnF₂ where x is a) 0, b) 0.08, c) 0.17, d) 0.25, e) 0.33, f) 0.42, g) 0.50, h) 0.58, i) 0.66, j) 0.75 and k) 0.83.

Table 6. 1: Reference XRD peaks and corresponding crystal planes converted from Cr radiation source to Cu radiation source, used to compare experimental results to reference data.

Formula	Cu Source (2 θ degrees)	Cr Source (2 θ degrees)	Crystal Plane
FA ₃ Bi ₂ I ₉	8.1	12.0	(002)
	16.1	24.0	(004)
	24.3	36.5	(006)
	41.0	62.7	(228)
	49.6	77.1	(319)
Cs ₃ Bi ₂ I ₉	8.5	12.7	(002)
	16.7	24.9	(004)
	25.3	38.0	(006)
	42.5	65.2	(228)
	51.8	81.0	(319)

Table 6. 2: Reference XRD peaks for precursor materials, converted to Cr-source peaks for comparison to experimental data.

CsI		BiI ₃		FAI		SbI ₃	
Cu source	Cr source	Cu Source	Cr Source	Cu Source	Cr Source	Cu Source	Cr Source
28.00	42.15	13.00	19.37	14.00	20.87	12.50	18.62
40.00	61.10	27.00	40.60	20.00	29.91	25.50	38.30
49.80	77.48	35.50	53.89	28.00	42.15	27.00	40.60
57.80	91.82	42.00	64.37	31.50	47.58	35.00	53.09
65.00	105.98	46.50	71.84	40.20	61.43	41.50	63.55
72.00	121.76	50.50	78.69	42.50	65.19	46.00	71.00
79.00	141.95	56.00	88.49	50.00	77.82	52.50	82.20